183
1-21-82

I-944

211

ornl

ORNL/TM--8063

DE82 007124

MASTER

OAK
RIDGE
NATIONAL
LABORATORY

UNION
CARBIDE

Finite-Beta Effects on the Nonlinear Evolution of the (m = 1;n = 1) Mode in Tokamaks

63

J. A. Holmes
B. A. Carreras
H. R. Hicks
V. E. Lynch
K. E. Rothe

OPERATED BY
UNION CARBIDE CORPORATION
FOR THE UNITED STATES
DEPARTMENT OF ENERGY

DISCLAIMER

Printed in the United States of America. Available from
National Technical Information Service
U.S. Department of Commerce
5285 Port Royal Road, Springfield, Virginia 22161
NTIS price codes—Printed Copy: A04; Microfiche A01

ORNL/TM-8063
Dist. Category UC-20 g

Contract No. W-7405-eng-26

FUSION ENERGY DIVISION

FINITE-BETA EFFECTS ON THE NONLINEAR EVOLUTION OF THE (m = 1;n = 1) MODE IN TOKAMAKS

J. A. Holmes

Computer Sciences

B. A. Carreras

Fusion Energy Division

H. R. Hicks, V. E. Lynch, and K. E. Rothe

Computer Sciences

Date Published - January 1982

NOTICE This document contains information of a preliminary nature. It is subject to revision or correction and therefore does not represent a final report.

Prepared by the
OAK RIDGE NATIONAL LABORATORY
Oak Ridge, Tennessee 37830
operated by
UNION CARBIDE CORPORATION
for the
DEPARTMENT OF ENERGY

DISTRIBUTION OF THIS DOCUMENT IS UNLIMITED

THIS PAGE

WAS INTENTIONALLY

LEFT BLANK

CONTENTS

THIS PAGE

WAS INTENTIONALLY

LEFT BLANK

ABSTRACT

The stability and evolution of ISX-B-like plasmas are numerically studied using a reduced set of resistive magnetohydrodynamic (MHD) equations. For a sequence of equilibria stable to ideal modes, the $n = 1$ mode changes from a tearing branch to a pressure-driven branch as β_p is increased. When this mode is unstable at low beta, it is just the $(m = 1; n = 1)$ tearing mode. Higher n modes also become linearly unstable with increasing β_p; they are essentially pressure driven and have a ballooning character. For low values of beta the instability is best described as a β_p distortion of the $(m = 1; n = 1)$ tearing mode. This mode drives many other helicities through toroidal and nonlinear couplings. As β_p is increased, the growth of the $m = 1$ island slows down in time, going from exponential to linear before reconnection occurs. If β_p is large enough, the island saturates without reconnection. A broad spectrum of other modes, driven by the $(m = 1; n = 1)$ instability, is produced. These results agree with some observed features of MHD activity in ISX-B.

1. INTRODUCTION

The $(m = 1;n = 1)$ tearing mode is believed to be responsible for the sawtooth oscillations[1] observed in ohmically heated tokamak discharges.[2] Recent experimental results from the neutral-beam-heated tokamak ISX-B show strong dependence of the magnetohydrodynamic (MHD) activity upon injection power.[3] For ohmic discharges the classical sawtooth behavior[1] is observed in soft x-ray signals. Very low beam powers $(P_b \lesssim P_{oh})$ affect the instability by enhancing the amplitude and period of this classical behavior, and a very weak coincident $\tilde{B}$ is observed at the Mirnov coils. As the beam power is increased $(P_b \gtrsim P_{oh})$, the instability signals are altered by a lengthening of the interval of $m = 1$ activity before internal disruption and by the simultaneous appearance of stronger $\tilde{B}$ at the same frequency as the $m = 1$. Further increases in beam power generally lead first to longer lived, even steadily running, precursors and then to increasing amplitude modulation of these signals. For discharges in which $P_b \gtrsim P_{oh}$ the x-ray and $\tilde{B}$ signals are locked in frequency and amplitude. The large x-ray signals are from within $q \approx 1$ and are due to a large $m = 1$ mode there. The $\tilde{B}$ at the Mirnov coils is strong, often exceeding $\tilde{B}/B = 1\%$, and is dominated by the $m/n = 2/1$ mode symmetry. Despite the large 2/1 $\tilde{B}$, there is no distinctive x-ray signal from near $q = 2$ and thus no large $m = 2$ island structure.

In order to understand the pattern of these results, we have numerically studied the effect of increasing beta on the stability and nonlinear evolution of the $(m = 1;n = 1)$ mode. The equations and numerical methods used for this study are discussed in Sect. 2; the equilibria we have considered are described in Sect. 3. With increasing β_p the $n = 1$ mode changes from a tearing mode to a pressure-driven mode (Sect. 4). As described in Sect. 5 this change in the linear eigenmode induces a change in the nonlinear behavior of this mode. In Sect. 6 we state our conclusions.

2. EQUATIONS AND NUMERICAL METHODS

The resistive MHD equations are

$$\rho_m\left(\frac{\partial\vec{v}}{\partial t} + \vec{v} \cdot \vec{\nabla}\vec{v}\right) = -\vec{\nabla}p + \vec{J} \times \vec{B} \quad , \tag{1}$$

$$\frac{\partial\vec{B}}{\partial t} = -\vec{\nabla} \times \vec{E} \quad , \tag{2}$$

$$\vec{J} = \frac{1}{\mu_o} \vec{\nabla} \times \vec{B} \quad , \tag{3}$$

and

$$\vec{E} = \eta\vec{J} - \vec{v} \times \vec{B} \quad , \tag{4}$$

where $\vec{v}$ is the fluid velocity, ρ_m is the mass density, p is the pressure, $\vec{B}$ is the magnetic field, $\vec{J}$ is the current density, $\vec{E}$ is the electric field, η is the resistivity, and μ_o is the vacuum magnetic permeability. In order to close this system of equations, it is necessary to specify an equation of state and equations for the resistivity and mass density. In this paper, the mass density is assumed to be constant in space and time and the resistivity to be constant in time. The equation of state is assumed to be

$$\frac{\partial p}{\partial t} + \vec{v} \cdot \vec{\nabla}p = -\Gamma p\vec{\nabla} \cdot \vec{v} \quad , \tag{5}$$

where Γ is the ratio of specific heats of the plasma.

A high-beta large aspect ratio tokamak ordering ($\beta \sim \varepsilon \equiv a/R_o \ll 1$) allows the reduction of the resistive MHD equations to a set of three partial differential equations in three unknowns.[4] Here, R_o is the plasma major radius and a is an average plasma minor radius given by

$$a^2 = \frac{R_o}{2\pi^2} \int_V R^{-2} dV \quad , \tag{6}$$

where the integration extends over the entire plasma volume. This ordering allows the toroidal component of the fluid velocity to be neglected and implies that the fluid is incompressible.

The reduced set of equations in dimensionless form is

$$\frac{\partial \Psi}{\partial t} + \vec{v}_\perp \cdot \vec{\nabla}\Psi = \frac{-\partial \Phi}{\partial \zeta} + \eta J_\zeta - E_{\zeta w} \quad , \tag{7}$$

$$\frac{\partial U}{\partial t} + \vec{v}_\perp \cdot \vec{\nabla} U = S^2 \left[\hat{\zeta} \cdot \left(\vec{\nabla} J_\zeta \times \vec{\nabla}\Psi \right) - \frac{\partial J_\zeta}{\partial \zeta} + \frac{\beta_o}{2\varepsilon^2 R} \hat{\zeta} \cdot \left(\vec{\nabla} \times R^2 \vec{\nabla} p \right) \right] \quad , \tag{8}$$

$$\frac{\partial p}{\partial t} + \vec{v}_\perp \cdot \vec{\nabla} p = 0 \quad , \tag{9}$$

with

$$U = \nabla_\perp^2 \Phi \tag{10}$$

and

$$J_\zeta = \Delta^* \Psi = R^2 \vec{\nabla}_\perp \cdot \left(\frac{1}{R^2} \vec{\nabla}_\perp \Psi \right) \quad , \tag{11}$$

where R is the major radius coordinate divided by R_o, β_o is the toroidal beta at the magnetic axis, and $\hat{\zeta}$ is a unit vector in the toroidal direction. All lengths are normalized to the generalized minor radius a, the resistivity to η_o (its value at the magnetic axis), the time to the resistive diffusion time $\tau_r = a^2\mu_o/\eta_o$, the magnetic field to $B_{\zeta o}$ (the unperturbed vacuum toroidal field at major radius R_o), the velocity to a/τ_r, and the pressure to p_o (its value at the magnetic axis). The functions Ψ and Φ are the poloidal flux and velocity stream functions, normalized to $a^2B_{\zeta o}$ and $a^2B_{\zeta o}/\tau_r$, respectively. They are related to the dimensionless magnetic field and fluid velocity by

$$\vec{B} = \frac{\varepsilon}{R}\,\hat{\zeta} \times \vec{\nabla}\Psi + \hat{\zeta} \tag{12}$$

and

$$\vec{v}_\perp = \vec{\nabla}\Phi \times \hat{\zeta} \quad , \tag{13}$$

where the subscript $\perp$ indicates perpendicularity to $\hat{\zeta}$. The toroidal current density is J_ζ/R and is normalized to $B_{\zeta o}/\mu_o R_o$, and U is the toroidal component of the vorticity. The parameter S is the ratio of the two time scales involved in this problem: $S = \tau_r/\tau_{hp}$, where τ_{hp} is the poloidal Alfvén time, $\tau_{hp} = R_o(\mu_o\rho_m)^{1/2}/B_{\zeta o}$. A conducting wall boundary condition is assumed along with zero pressure at the plasma edge.

Equations (7)-(9) are numerically advanced in time using the three-dimensional nonlinear initial value resistive MHD code RST. Axisymmetric toroidal numerical equilibrium solutions are calculated using the RSTEQ equilibrium code.[5] Even though Eqs. (7)-(9) keep dynamical terms only to lowest order in ε, the solution of the Grad-Shafranov equation (exact to all orders in ε),

$$\Delta^{*}\Psi = -\frac{\beta_o}{2\varepsilon^2} R^2 \frac{dp}{d\Psi} - \frac{1}{\varepsilon^2} F \frac{dF}{d\Psi} \quad , \tag{14}$$

where $F = RB_\zeta$, is an equilibrium solution for the $\eta \to 0$ limit of these equations. Assuming zero velocity at equilibrium, Eq. (9) becomes identically zero, and Eq. (8) can be shown to be zero from force balance,

$$\vec{J} \times \vec{B} = \frac{\beta_o}{2\varepsilon} \vec{\nabla} p \quad , \tag{15}$$

by operating on both sides of Eq. (15) with the operator L defined by $L(f) \equiv \hat{\zeta} \cdot (\vec{\nabla} \times R^2 f)$.

The equations are solved in a generalized nonorthogonal flux coordinate system (ρ, Θ, ζ)[6,7] determined by the equilibrium. In this system ρ $(0 \leqslant \rho \leqslant 1)$ is an equilibrium flux surface variable which behaves as a generalized minor radius, Θ $(0 \leqslant \Theta \leqslant 2\pi)$ is a generalized poloidal angle variable, and ζ is the toroidal angle. The particular choice of coordinates employed in this work is determined by setting the Jacobian such that

$$D \equiv \frac{1}{R} \left(\frac{\partial X}{\partial \rho} \frac{1}{\rho} \frac{\partial Z}{\partial \Theta} - \frac{1}{\rho} \frac{\partial X}{\partial \Theta} \frac{\partial Z}{\partial \rho} \right)^{-1} = R^{-2} \quad , \tag{16}$$

where $X = (R - 1)/\varepsilon$ and Z are horizontal and vertical dimensionless minor radius coordinates, respectively. Expressing each dynamical quantity f in terms of an equilibrium contribution f_{eq} and a perturbation contribution $\tilde{f}$ and noting that $\vec{v}_{\perp eq} = \Phi_{eq} = U_{eq} = 0$, Eqs. (7)-(9) in the generalized coordinate system become

$$\frac{\partial \tilde{\Psi}}{\partial t} = -\frac{1}{\rho}\frac{\partial \Phi}{\partial \Theta}\frac{d\Psi_{eq}}{d\rho} - \frac{\partial \Phi}{\partial \zeta} + \frac{\partial \Phi}{\partial \rho}\frac{1}{\rho}\frac{\partial \tilde{\Psi}}{\partial \Theta} - \frac{1}{\rho}\frac{\partial \Phi}{\partial \Theta}\frac{\partial \tilde{\Psi}}{\partial \rho} + \eta \tilde{J}_\zeta \quad , \tag{17}$$

$$\begin{aligned}\frac{\partial U}{\partial t} = {} & \frac{\partial \Phi}{\partial \rho}\frac{1}{\rho}\frac{\partial U}{\partial \Theta} - \frac{1}{\rho}\frac{\partial \Phi}{\partial \Theta}\frac{\partial U}{\partial \rho} + S^2 \left[\frac{\partial J_{\zeta eq}}{\partial \rho}\frac{1}{\rho}\frac{\partial \tilde{\Psi}}{\partial \Theta}\right. \\ & - \frac{1}{\rho}\frac{\partial \tilde{J}_\zeta}{\partial \Theta}\frac{d\Psi_{eq}}{d\rho} - \frac{1}{\rho}\frac{\partial J_{\zeta eq}}{\partial \Theta}\frac{\partial \tilde{\Psi}}{\partial \rho} - \frac{\partial \tilde{J}_\zeta}{\partial \zeta} + \frac{\partial \tilde{J}_\zeta}{\partial \rho}\frac{1}{\rho}\frac{\partial \tilde{\Psi}}{\partial \Theta} \\ & \left. - \frac{1}{\rho}\frac{\partial \tilde{J}_\zeta}{\partial \Theta}\frac{\partial \tilde{\Psi}}{\partial \rho} + \frac{\beta_0}{\varepsilon}\left(\frac{1}{R}\frac{\partial X}{\partial \rho}\frac{1}{\rho}\frac{\partial \tilde{p}}{\partial \Theta} - \frac{1}{R\rho}\frac{\partial X}{\partial \Theta}\frac{\partial \tilde{p}}{\partial \rho}\right)\right] \quad ,\end{aligned} \tag{18}$$

and

$$\frac{\partial \tilde{p}}{\partial t} = -\frac{1}{\rho}\frac{\partial \Phi}{\partial \Theta}\frac{dp_{eq}}{d\rho} + \frac{\partial \Phi}{\partial \rho}\frac{1}{\rho}\frac{\partial \tilde{p}}{\partial \Theta} - \frac{1}{\rho}\frac{\partial \Phi}{\partial \Theta}\frac{\partial \tilde{p}}{\partial \rho} \quad . \tag{19}$$

The linear operator Δ^* in this coordinate system is

$$\begin{aligned}\Delta^* f \equiv {} & \frac{1}{\rho}\frac{\partial}{\partial \rho}\left(g^{\rho\rho}\,\rho\frac{\partial f}{\partial \rho} + \rho g^{\rho\Theta}\,\frac{1}{\rho}\frac{\partial f}{\partial \Theta}\right) \\ & + \frac{1}{\rho}\frac{\partial}{\partial \Theta}\left(g^{\Theta\rho}\,\frac{\partial f}{\partial \rho} + g^{\Theta\Theta}\,\frac{1}{\rho}\frac{\partial f}{\partial \Theta}\right) \quad .\end{aligned} \tag{20}$$

The quantities $g^{\rho\rho}$, $g^{\rho\Theta} = g^{\Theta\rho}$, and $g^{\Theta\Theta}$ are the metric elements of the generalized coordinate system expressed in terms of toroidal (X,ϕ,Z) coordinates:

$$g^{\rho\rho} = \left(\frac{1}{R\rho}\frac{\partial X}{\partial \Theta}\right)^2 + \left(\frac{1}{R\rho}\frac{\partial Z}{\partial \Theta}\right)^2 \quad , \tag{21}$$

$$g^{\rho\Theta} = -\left(\frac{1}{R\rho}\frac{\partial X}{\partial \Theta}\frac{1}{R}\frac{\partial X}{\partial \rho} + \frac{1}{R\rho}\frac{\partial Z}{\partial \Theta}\frac{1}{R}\frac{\partial Z}{\partial \rho}\right) \quad , \tag{22}$$

and

$$g^{\Theta\Theta} = \left(\frac{1}{R}\frac{\partial X}{\partial \rho}\right)^2 + \left(\frac{1}{R}\frac{\partial Z}{\partial \rho}\right)^2 \quad . \tag{23}$$

Equations (17)-(19) make use of the fact that Ψ_{eq} and p_{eq} are functions of ρ only.

The above equations are solved by using a finite difference representation in the radial coordinate ρ and Fourier series expansion in the angle variables Θ and ζ.[8] In terms of this representation, quantities dependent upon the equilibrium are written

$$f_{cq}(\rho,\Theta) = \sum_{m=0}^{\infty} \left[f^c_{cqm}(\rho)\cos m\Theta + f^s_{cqm}(\rho)\sin m\Theta\right] \quad , \tag{24}$$

whereas perturbation quantities are written

$$\tilde{f}(\rho,\Theta,\zeta) = \sum_{n=0}^{\infty} \sum_{m=-\infty}^{\infty} \left[f^c_{mn}(\rho)\cos(m\Theta + n\zeta) + f^s_{mn}(\rho)\sin(m\Theta + n\zeta)\right] \quad . \tag{25}$$

Although RST allows both sine and cosine terms, we restrict our study to equilibria having up-down symmetry (cosine terms only). Then, in cases where only the cosine terms in Ψ are initialized, the sine terms in Ψ, J_ζ, and p and the cosine terms in Φ and U remain zero. In order to simplify the presentation, only this latter situation will be discussed, and the superscripts c and s will be dropped. In practice the series in Eqs. (24)-(25) must be truncated at a finite number of modes. The resistivity η is taken to be a function of ρ only and is defined by $\eta\langle J_{\zeta eq}\rangle = E_{\zeta w}$, where $E_{\zeta w}$ is assumed to be constant and the $\langle\ \rangle$ means average over equilibrium flux surfaces. With this choice of resistivity the equilibrium is an approximate resistive equilibrium.

Equations (17)-(19) explicitly exhibit the linear and nonlinear terms in the moderate-beta reduced equations. By omitting or including the nonlinear terms the RST code can be used either for the study of linear stability or as a full nonlinear initial value code. Both modes of operation are used in this work.

Most of the numerical techniques used in this work are derived from the RSF code.[8] However, two differences between RST and RSF should be mentioned. The first is the addition of the pressure convective equation (19) in RST. In order to numerically advance this equation in the nonlinear regime, a small diffusion term $\chi\Delta^{*}\tilde{p}$ is added to the right-hand side. Numerical schemes involving noncentered spatial derivatives, which are usually applied to the solution of convective equations, are difficult to implement in the mixed Fourier-finite difference representation used here. The diffusion coefficient χ is small enough to have no effect on the linear growth rate of the modes under study. A second difference is in the form of the matrices required to calculate the inversion of $U = \Delta_{\perp}^{2}\Phi$ and the implicit diffusion terms due to $\eta\Delta^{*}\Psi$ in Eq. (17) and $\chi\Delta^{*}\tilde{p}$, which is added into Eq. (19). Because the equilibria for RST lack poloidal symmetry, Fourier components having a given toroidal mode number n but different poloidal mode numbers m are linearly coupled through the equilibrium quantities. Using a three-point second-order radial difference scheme, a block tridiagonal matrix having MJ rows of blocks (MJ being the number of radial grid points) with each block of size M(n) × M(n), where M(n) is the number of poloidal components of toroidal mode number n in the calculation, must be inverted for each toroidal mode number n in each of the three operations alluded to above. In addition to adding complexity to the matrix structure for the Δ^* and related operators, these geometric couplings necessitate the inclusion of a greater number of Fourier components in order to represent the modes. This has the effect of shortening the time step size used by RST as can be seen from the formula

$$\Delta t \lesssim \frac{2}{S\ \mathrm{Max}\left| n - \frac{m}{q(\rho)} \right|} \quad , \qquad (26)$$

which results from a simplified von Neumann stability analysis of Eqs. (17)-(18). Here, $q(\rho)$ is the equilibrium safety factor q profile.

In RST the block tridiagonal matrix solutions require more computer time than any other part of the code. Because of the large number of Fourier components, the shortness of the time step, and the dominance of the matrix equations in computer time, it is essential to use efficient software for their solution. RST solves the matrix equations using the block tridiagonal matrix package BT/BTMS.[9]

3. EQUILIBRIA

The equilibria used in this study are numerical solutions of the toroidal axisymmetric Grad-Shafranov equation (14). They are calculated in a flux conserving manner with a pressure profile $p_{eq} \propto \Psi^2_{eq}(\rho)$ and a safety factor profile parameterized as $q = q_o[1 + (\rho/\rho_o)^4]^{1/2}$. We have studied several such sequences of equilibria. The detailed parameters for one of those sequences are given in Table 1. In the low-beta cylindrical limit for this particular q profile only, the (m = 1;n = 1) tearing mode is unstable.

Since a detailed simulation of the ISX-B experiment has not been attempted at this point, equilibria which accurately match the experimental parameters have not been sought. The flux conserving sequence of equilibria shown in Table 1 was chosen to allow a systematic study of the linear and nonlinear behavior of the (m = 1;n = 1) tearing mode as a function of beta. The systematics of this behavior can be compared with those of the ISX-B experiment described in the Introduction. Other equilibrium sequences (Table 2) are used to study the effects of changing q_a and q_o. We have not studied the effects of varying the pressure profile but have maintained $p_{eq} \propto \Psi^2_{eq}$ throughout these calculations.

As beta is increased in a flux conserving manner, the equilibrium geometry becomes distorted away from circularity except at the boundary. The toroidal current distribution and equilibrium flux surfaces shift outward in major radius as seen in Fig. 1. The peak of the current density shifts relative to the magnetic axis. This modifies the current gradient at the q = 1 surface (see Fig. 2 and

Table 1) in a way which tends to stabilize the tearing mode. This behavior is a consequence of the flux conserving method, which is probably optimal for stability of tearing modes. Although the RST code allows the study of plasmas of more general cross section, the equilibria considered here are for circular cross-section plasmas. The effects of noncircularity on the stability of high-beta plasmas are under study at present.

4. LINEAR PROPERTIES OF THE n = 1 EIGENMODE

A linear study of the n = 1 eigenmode was carried out for the flux conserving sequence of equilibria described in Table 1. The survey was conducted at $S = 10^5$, as were all calculations in this paper, unless otherwise noted. In order to separate the beta effects of the dynamical pressure driving term in Eq. (18) from those induced by the equilibrium, linear calculations were carried out in two ways: (1) using linearized versions of the full equations and (2) using the same equations with the dynamical pressure term in Eq. (18) turned off. In the first method pressure-driven and current-driven effects are included, whereas in the second method only current-driven effects are allowed. Beta effects observed using the second method of calculation are caused by the distortion of the equilibrium geometry, whereas the first method also includes the dynamical effects of the pressure terms.

The n = 1 linear growth rate is plotted as a function of β_p for both methods in Fig. 3. The dashed curve, which was calculated without dynamical pressure effects, illustrates the effect of beta induced by the equilibrium upon the stability of the current-driven mode. As described in Sect. 3, the shift of the peak of the toroidal current relative to the magnetic axis decreases the current gradient at the q = 1 surface. It also increases the coupling to other modes, which are stable; both effects tend to stabilize the mode. The solid curve was calculated using the full linearized equations, and it therefore includes pressure-driven dynamical effects in addition to those of the other curve. For low values of β_p the pressure terms produce an interchange stabilization of the $n = 1$ mode similar to that predicted by Glasser et al.,[10] but as β_p increases, the character of the mode changes, becoming mainly pressure driven with an increasingly large growth rate.

The effects of beta upon the $n = 1$ mode when dynamical pressure effects are included are illustrated in Fig. 4 (which shows the $m = 1$ Fourier components of Ψ, p, and Φ at $\beta_p = 0.19, 0.59, 1.00$, and 1.94, respectively). The similarity between the p and Φ components is expected from the linearized form of the dynamical pressure equation;

$$\gamma_n p_{mn} = - \frac{m}{\rho} \phi_{mn} \frac{dp_{eq}}{d\rho} \quad , \tag{27}$$

where γ_n is the linear growth rate.

The relative magnitudes of p_{mn} and ϕ_{mn} are consistent with this expression. For $\beta_p = 0.19$ the ψ_{11} component is dominant and has the typical kink mode structure obtained in the low-beta limit, indicating that the $n = 1$ eigenmode is mainly a current-driven mode. At $\beta_p = 1.94$, the $n = 1$ mode is mainly pressure driven and its Fourier components are localized near the $q = 1$ singular surface. This particular equilibrium is stable to the $n = 1$ mode when the β/ε term is removed from Eq. (18), as indicated by the dashed curve of Fig. 3. For $\beta_p = 0.59$ and 1.00, Fig. 4 shows the transition from current- to pressure-driven dominance.

A large number of Fourier components is necessary to correctly describe an eigenmode when the beta effects are included. We have found that the coordinate system we use is optimal in minimizing the number of components. However, about ten poloidal components are required to calculate the linear growth rates accurately to within a few percent. In Fig. 5 we show the different poloidal components of Ψ used in calculating the linear n = 1 eigenmode for two values of β_p, $\beta_p = 0.19$ (Fig. 5a) and $\beta_p = 1.94$ (Fig. 5b). For the lower value of β_p, all modes show a global character which is normally associated with kink modes. The m = 2 component is the largest of the driven components, and its structure is quite different from a linearly unstable (m = 2;n = 1) tearing mode. This component peaks near the q = 1 singular surface and has hardly any structure near the q = 2 surface. The observed structure carries over in the nonlinear regime with important observable consequences as we will show in the next section. At the highest value of β_p (Fig. 5b), the structure of the components is considerably different, as already seen for the (m = 1;n = 1) in Fig. 4. All components are highly localized near the q = 1 surface, and the m = 1 component is no longer dominant; both the m = 0 and m = 2 components have larger amplitudes than the m = 1.

To estimate the relative amplitudes of different Fourier components, we define for each component a magnetic energy norm

$$(E_M)_{mn} = \frac{1}{2}\int_o^1 \rho\, d\rho \left[\left(\frac{\partial\psi_{mn}}{\partial\rho}\right)^2 + \left(\frac{m\psi_{mn}}{\rho}\right)^2\right] \qquad (28)$$

and a pressure norm

$$(E_P)_{mn} = \int_o^1 \rho\, d\rho\, p_{mn} \quad . \qquad (29)$$

The ratio of the magnetic energies in the m = 2 and m = 3 components to that in the m = 1 component is shown as a function of β_p in Fig. 6 for cases both with (solid curves) and without (dashed curves) dynamical pressure effects. When dynamical pressure effects are excluded, the change in strength of the current-driven components, which is due to the increasing deformation of the current profile relative to the flux surfaces, is gradual and continuous. For cases with dynamical pressure effects included, the relative strengths of the high m components increase more rapidly as the mode shifts from current to pressure driven. A saturation of the relative $m = 2$ and $m = 3$ magnetic energies occurs after the mode is essentially in the pressure-driven regime. Figure 7a illustrates this discussion for a whole range of components by plotting the ratio of the (m;1) and (1;1) magnetic energies for values of $\beta_p = 0.07$, 0.19, 0.38, 0.59, and 1.00. The similarity between the $\beta_p = 0.59$ and 1.00 magnetic energy spectra shows the saturation effect mentioned above. This figure also illustrates that for the coordinate system used the number of poloidal components necessary to accurately represent an eigenfunction is not a strong function of β_p.

The results presented so far illustrate β_p effects on the stability of the $n = 1$ mode for a particular flux conserving sequence of equilibria. In order to assess the effects of modifying the q profile, linear stability calculations were made for the flux conserving sequences described in Table 2. For each of the flux conserving sequences considered, two regimes emerged: a low β_p regime in which the current-driven effects dominate and a high β_p regime in which pressure-driven effects dominate. In the low β_p regime the $n = 1$ mode is essentially a tearing mode modified by β_p effects. The structure and growth of the mode in this regime are determined mainly by the equilibrium current, with the pressure driving terms enhancing the couplings and providing some degree of stabilization. In the high β_p regime the effects of the q profile diminish as the mode becomes mainly pressure driven. This is illustrated in Fig. 8, which plots the n = 1 linear growth rates as functions of β_o and β_p for the three equilibrium sequences considered. At high β_p, where pressure driving effects dominate, the growth rates are seen to be nearly independent of the q profile. This is not true for the β_o plot, so that the growth rate in the high-beta regime can be expressed better as a function of β_p than β_o. However, at low β_p the growth rates are stronger functions of the q profile. Noting that the (m = 1;n = 1) tearing mode in the low-beta limit is driven by the shear at the q = 1 surface, it is interesting that $\left.\frac{\rho}{q}\frac{dq}{d\rho}\right|_{q=1} = 0.38, 0.39$, and 0.72 for the $q = 0.9 \rightarrow 2.3$, $q = 0.9 \rightarrow 3.3$, and $q = 0.8 \rightarrow 2.3$ profiles, respectively. This explains the enhancement of the growth rate at low β_p for the latter profile. The transition region from current- to pressure-driven dominance is q profile dependent, with current driving effects lingering to higher β_p for profiles having greater shear.

The difference between the growth rates of the $q = 0.9 \rightarrow 2.3$ and $q = 0.9 \rightarrow 3.3$ profiles at low β_p is at least partially due to the relative stability of the driven (m = 2;n = 1) and (m = 3;n = 1) modes for these cases. For the latter profile the m = 3 is resonant and the m = 2 is unstable in the low β_p limit, whereas for the former profile the m = 3 is nonresonant and the m = 2 is stable. This is illustrated in Fig. 7 where, comparing the $\beta_p = 1.00$ magnetic energy distribution in 7a with that for $\beta_p = 1.02$ in 7b, the enhancement of the magnetic energy of the m = 3 component is obvious for the $q = 0.9 \rightarrow 3.3$ profile, for which the (m = 3;n = 1) component is resonant in the plasma.

Higher n modes, which are stable at low beta, become linearly unstable with increasing beta.[11] They are essentially pressure driven, and their linear growth rate increases strongly with beta (Fig. 9). The linear growth rate (at high values of beta) increases with n, and the structure of the eigenfunctions has ballooning character.

In summary, β_p modifications to the n = 1 mode are induced by distortion of the equilibrium current profile, which changes the growth rate and couples components having different m values, and by the transition from current to pressure as the driving term of the instability.

5. NONLINEAR RESULTS

Nonlinear calculations of the plasma evolution were carried out for the flux conserving equilibrium sequence shown in Table 1, up to the $\beta_p = 1$ case. These cases cover the range in which the n = 1 linear eigenmode changes from a classical tearing mode to a more complex mode structure for which the pressure driving terms are important (Fig. 4). Approximately 50 Fourier components having toroidal mode numbers in the range n = 0, . . . , 7 were included in these calculations. For higher values of β_p, the large n modes are linearly unstable, with growth rates increasing with n (Fig. 9). This makes nonlinear numerical calculations based on Fourier expansions difficult. In such cases, it is necessary to include terms in the equations that simulate effects, such as finite Larmor radius corrections, which limit the range of unstable n values and allow a correct evaluation of these modes. However, even taking such effects into account, the computations are slow and very lengthy. We have not yet obtained reliable results for these high β_p equilibria.

The main results of the nonlinear studies can be summarized as follows:

(1) For the equilibrium sequence in Table 1 and $\beta_p \lesssim 0.5$, the nonlinear growth of the m = 1/n = 1 magnetic island slows down with increasing β_p, going from exponential to linear prior to reconnection.

(2) For higher values of β_p, the m = 1/n = 1 magnetic island saturates and remains at a finite amplitude. This transition from

reconnection to saturation happens when the mode becomes dominantly pressure driven.

(3) The $(m = 1;n = 1)$ mode drives many modes through toroidal and nonlinear coupling. The largest driven mode for this equilibrium sequence is the $(m = 2;n = 1)$ mode. This mode, as discussed in Sect. 4, is mainly localized near the $q = 1$ surface, and the induced $m = 2/n = 1$ magnetic island is small. However, the $(m = 2;n = 1)$ mode produces a large poloidal magnetic field perturbation at the plasma surface.

(4) A broad spectrum of other driven modes is produced. These generate a variety of magnetic islands that in many cases overlap and break the magnetic surfaces.

The first two results are shown in detail in Fig. 10. In this figure we have plotted the time evolution of the $m = 1/n = 1$ magnetic island width (top) and the $(m = 2;n = 1)$ component of the poloidal magnetic field at the plasma edge for the different equilibria we have considered. The dashed curve shows the result for the low-beta cylindrical equilibrium with the same q profile. In this limit the $m = 1/n = 1$ magnetic island grows exponentially with time, flattening the current and q profiles. The magnetic field line topology flips, with the center of the island becoming the new magnetic axis, and after magnetic field line reconnection, the cylindrical symmetry is recovered with $q > 1$ in the whole plasma volume. This nonlinear process was theoretically anticipated by Kadomtsev[12] and studied numerically in detail in Refs. 13-15. As already mentioned, an effect of increasing beta upon the nonlinear evolution is to lengthen the time until magnetic field line reconnection. This stretching out of the nonlinear evolution of the $m = 1/n = 1$ island width is due to a period of linear, rather than exponential, growth in time. This is quite evident in the case of $\beta_p = 0.38$ (Fig. 10). This behavior is similar to that of the $m > 1$ tearing modes in cylindrical geometry[16] and is probably induced by the strong coupling of the $m = 1$ to $m > 1$ modes. For $\beta_p = 0.59$, Fig. 10 shows that the $m = 1/n = 1$ magnetic island saturates at a width $W \simeq 0.1a$. The saturation of the $(m = 1;n = 1)$ mode in high temperature, low-beta cylindrical plasmas has been predicted by Biskamp,[17] who included diamagnetic drifts, ion viscosity, plasma diffusion, and resistivity in a single helicity calculation. In his calculations saturation occurs when the $(m = 1;n = 1)$ linear growth rate is exceeded by the diamagnetic drift frequency ω_*. For high-beta plasmas this effect could be important in modifying the threshold of the saturation of the $(m = 1;n = 1)$ mode.

Let us now consider the nonlinear evolution in detail. We will describe first a case in which the $m = 1/n = 1$ island induces full reconnection of magnetic field lines and second a case in which the $m = 1/n = 1$ island saturates. Figures 11-13 show magnetic field line plots, pressure profiles, and pressure contour plots, respectively, at several times for a case in which there is full reconnection of magnetic field lines ($\beta_p = 0.38$). The field line plots in Fig. 11 show the evolution of the $m = 1/n = 1$ island toward reconnection. At $t = 1398\tau_{hp}$ the $m = 1/n = 1$ island width has reached nearly 20% of the plasma minor radius. Other modes are driven by the $(m = 1;n = 1)$ through toroidal and nonlinear coupling. These modes generate magnetic islands of different helicities, as can be seen in the figure.

At the later times two interesting features are observed: (1) the 1/1 island grows, squeezing the original magnetic axis into a small region to the left of the island (a hot spot), and (2) the interaction between modes becomes sufficiently large that many driven magnetic islands overlap, causing the magnetic field lines to become stochastic in certain regions of the plasma.

The pressure profile flattens inside the 1/1 island (Figs. 12-13). As the 1/1 grows, the region of flat pressure increases with the size of the island. At $t = 1967\tau_{hp}$, a local pressure peak (hot spot) remains to the left of the island at the present location of the magnetic axis, but the bulk of the plasma center, which is occupied by the 1/1 island, displays a flat pressure profile.

For higher values of β_p the $m = 1/n = 1$ island saturates. In particular, for $\beta_p = 0.59$, the $(m = 1;n = 1)$ mode couples to other modes which generate several magnetic islands, but the instability saturates when the $m = 1/n = 1$ island has a width $W \gtrsim 0.1a$ (Fig. 14). In this case, all the $n > 1$ modes used in the calculation are linearly unstable. Therefore, some of the magnetic islands present in the plasma are not driven by this mode. The effect of these high n pressure-driven modes upon the low n evolution for $\beta_p < 1$ cases considered in this sequence is small. These high n modes are observed to saturate at small amplitudes for realistic values of S ($S \gtrsim 10^6$).

If the value of S is unrealistically low ($S \sim 10^4$), the high n modes evolve very fast and generate a singularity in the pressure. Since we are below the threshold of the ideal instability, increasing S reduces the instability, and, for $S \gtrsim 10^5$, the modes saturate without presenting this singular behavior.

The value of S also affects the evolution of the low n modes (Fig. 15). For a reconnection case, as S increases the growth of the 1/1 island is significantly stretched out in time. In ISX-B the poloidal Alfvén time and magnetic Reynolds number are $\tau_{hp} \approx 0.4$ μs and $S \approx 10^7$, respectively. Assuming a power law dependence of τ_{recon}, the time for the evolution of the (m = 1;n = 1) mode to reconnection, upon S, and then the extrapolation of τ_{recon} in Fig. 15 (for the $\beta_p = 0.19$ case in Table 1) indicates that $\tau_{recon} \approx 10{,}000\tau_{hp}$ for $S = 10^7$. This corresponds to a (m = 1;n = 1) mode evolution time of several milliseconds for such a case in ISX-B, which is in good qualitative agreement with the observed duration of m = 1 precursors for low beam power ISX-B cases.

Hence, the effects of increasing β_p on the evolution of the m = 1 mode for a flux conserving sequence of equilibria lead to an interpretation consistent with ISX-B observations.[3] Associating the nonlinear evolution of the (m = 1;n = 1) mode with the observed MHD activity, both the calculations and the experiment observe with increasing β_p the slowing down of the classical sawtooth oscillation, the transition to a long or steadily running precursor signal (saturated 1/1 island), and the occurrence of sizeable m = 2 $\tilde{B}/B$ signals at the plasma edge with at most a small associated 2/1 magnetic island. Also, extrapolation of the time scales of the reconnection process in the calculations to ISX-B parameters is consistent with experimental observations.

As with linear stability, the effects of modifying the q profile have important consequences for $\beta_p \lesssim 1$ in the nonlinear regime. Increasing B_T for fixed plasma current, density, and beam power P_b in

ISX-B leads to an increase in q_a. In this process β_p is observed to remain constant while the behavior of the m = 1 returns to the "classical" sawtooth with a speeding up of the nonlinear evolution and a reduction of coupling to the driven modes, as evidenced by a reduced $\tilde{B}/B$ signal. This behavior is observed in our calculations, as shown in Fig. 16 where two equilibria, from Tables 1 and 2, having comparable β_p but different q_a are seen to have markedly different reconnection times. The case with $q_a = 3.3$ undergoes field line reconnection much more rapidly than the $q_a = 2.3$ case. The plots of the $(m = 2;n = 1)$ poloidal magnetic perturbation at the plasma edge reveal a much larger signal for the $q_a = 2.3$ case than for the $q_a = 3.3$ case, indicating that the $(m = 2;n = 1)$ mode is driven less by the $(m = 1;n = 1)$ in the latter case than in the former.

Increasing the shear at the q = 1 surface by decreasing q_o can also affect the nonlinear evolution, as can be seen in Fig. 17. Here again, for two cases from Tables 1 and 2 with comparable β_p but different q_o, the island widths and $(m = 2;n = 1)$ poloidal magnetic perturbations at the plasma edge are plotted as functions of time. The higher shear case with $q_o = 0.8$ undergoes fairly rapid magnetic field line reconnection, whereas the $q_o = 0.9$ case displays a saturated $(m = 1/n = 1)$ island. Hence, the evolution of the $(m = 1;n = 1)$ mode in a moderate-beta plasma can be quite sensitive to changes in the q profile.

6. CONCLUSIONS

The stability and nonlinear evolutions of the (m = 1;n = 1) mode in high-beta plasmas have been studied as functions of β_p for several flux conserving sequences of ideal MHD stable equilibria. A linear stability study of this mode for a flux conserving sequence of equilibria displays a transition from a mainly current-driven tearing mode at low β_p to a mainly pressure-driven mode at high β_p. As β_p is increased, the current-driven n = 1 mode is at first stabilized by equilibrium β_p and interchange stabilization effects in which the dominant (m = 1;n = 1) component is coupled to more stable m components. In this regime the structure of the n = 1 mode is essentially that of a modified low-beta (m = 1;n = 1) tearing mode. As β_p is increased further, the n = 1 mode becomes mainly a pressure-driven mode. The transition region from current- to pressure-driven dominance is sensitive to the q profile. Higher n modes, which are all stable at very low β_p, are linearly destabilized when β_p increases, having growth rates which increase with both β_p and n.

Nonlinear calculations thus far have been carried out for β_p up to about 1. As β_p is increased, the "classical" field line reconnection of the (m = 1;n = 1) mode becomes stretched out in time, and a period of linear magnetic island growth emerges prior to reconnection. For the higher values of β_p considered here, the m = 1/n = 1 island saturates. The equilibrium-induced couplings of the (m = 1;n = 1) drive other m components which give substantial $\tilde{B}/B$ values at the plasma edge. As β_p enters the pressure-driven regime higher n modes become linearly unstable and generate many small islands, some of which can overlap and cause certain regions of the plasma to become stochastic. Increasing q_a tends to speed up this evolution and decouple the driven modes from the $(m = 1;n = 1)$, causing the return to the "classical" $(m = 1;n = 1)$ behavior. Decreasing q_o tends to increase the shear at the $q = 1$ surface, which also speeds up the nonlinear evolution.

It is clear that these results can explain some of the observed MHD behavior in the ISX-B tokamak as described in the Introduction. These results are subject to the condition that $q_o < 1$, and the details of the evolution for any particular case are sensitive to the choice of equilibrium q profile. A detailed discussion of the MHD activity in ISX-B and its interpretation in terms of these calculations is forthcoming.[3]

ACKNOWLEDGMENTS

We thank our colleagues of the ISX-B experimental team, particularly J. L. Dunlap, V. K. Paré, and A. P. Navarro, for their collaboration in the study of MHD activity in ISX-B, for providing a wealth of experimental data against which to compare our calculations, and for useful discussions throughout this work.

REFERENCES

1. S. von Goeler, W. Stodiek, and N. Sauthoff, Phys. Rev. Lett. 33, 1201 (1974).

2. G. L. Jahns, M. Soler, B. V. Waddell, J. D. Callen, and H. R. Hicks, Nucl. Fusion 18, 609 (1978).

3. J. L. Dunlap, B. A. Carreras, V. K. Paré, J. A. Holmes, S. C. Bates, J. D. Bell, H. R. Hicks, V. E. Lynch, and A. P. Navarro, "MHD Instability with Neutral Beam Heating in the ISX-B Tokamak" (unpublished).

4. H. R. Strauss, Phys. Fluids 20, 1354 (1977).

5. J. A. Holmes, Y-K. M. Peng, and S. J. Lynch, J. Comput. Phys. 36, 35 (1980).

6. R. C. Grimm, J. M. Green, and J. L. Johnson, in Methods of Computational Physics, Academic Press, New York, Vol. 16, 253 (1976).

7. B. Carreras, H. R. Hicks, D. K. Lee, Phys. Fluids 24, 66 (1981).

8. H. R. Hicks, B. A. Carreras, J. A. Holmes, D. K. Lee, and B. V. Waddell, "3-D Nonlinear Calculations of Resistive Tearing Modes," J. Comput. Phys. (to be published).

9. A. C. Hindmarsh, "Solution of Block-Tridiagonal Systems of Linear Algebraic Equations," Lawrence Livermore National Laboratory Report UCID-30150 (February 1977).

10. A. H. Glasser, J. M. Green, and J. L. Johnson, Phys. Fluids 18, 875 (1975).

11. H. R. Hicks, J. A. Holmes, B. A. Carreras, D. J. Tetreault, G. Berge, J. P. Freidberg, P. A. Politzer, and D. Sherwell, Plasma Physics and Controlled Nuclear Fusion Research 1980, Vol. I, 259 (1981).

12. B. B. Kadomtsev, Sov. J. Plasma Phys. 1, 710 (1975).

13. A. F. Danilov, Yu N. Dnestrovskii, D. P. Kostomarov, and A. M. Popov, Sov. J. Plasma Phys. 2, 167 (1976).

14. A. Sykes and J. A. Wesson, Phys. Rev. Lett. 37, 140 (1976).

15. B. V. Waddell, M. N. Rosenbluth, D. A. Monticello, and R. B. White, Nucl. Fusion 16, 528 (1976).

16. P. H. Rutherford, Phys. Fluids 16, 1903 (1973).

17. D. Biskamp, Phys. Rev. Lett. 46, 1522 (1981).

Table 1. Detailed equilibrium parameters for a flux conserving sequence characterized by

$\varepsilon = 0.25$ $p = [\Psi_{eq}(\rho)/\Psi_{eq}(o)]^2$ $q_o = 0.9$ $q_a = 2.3$

β_p	β_o(%)	$\langle\beta\rangle$(%)	Magnetic axis shift	$\left(\frac{\partial J_{oo}}{\partial \rho}\right)_{q=1}$
0.07	0.3	0.09	0.06a	4.01
0.19	1.0	0.25	0.07a	3.95
0.38	2.0	0.53	0.09a	3.86
0.59	3.1	0.84	0.12a	3.77
1.00	5.6	1.51	0.17a	3.56
1.49	8.7	2.41	0.23a	3.29
1.94	12.1	3.40	0.28a	3.03

Table 2. Equilibrium parameters for the three flux conserving sequences used in this paper

$\varepsilon = 0.25$ $\quad p = [\Psi_{eq}(\rho)/\Psi_{eq}(0)]^2$ $\quad q = q_o \sqrt{1 + (\rho/\rho_o)^4}$

β_o(%)	$q_o = 0.9$ $q_a = 2.3$		$q_o = 0.9$ $q_a = 3.3$		$q_o = 0.8$ $q_a = 2.3$	
	β_p	Magnetic axis shift	β_p	Magnetic axis shift	β_p	Magnetic axis shift
0.3	0.07	0.06a	0.12	0.07a	0.06	0.05a
1.0	0.19	0.07a	0.34	0.09a	0.18	0.07a
2.0	0.38	0.09a	0.68	0.13a	0.37	0.09a
3.1	0.59	0.12a	1.02	0.16a	0.57	0.11a
5.6	1.00	0.17a	1.67	0.23a	0.98	0.16a
8.7	1.49	0.23a	2.33	0.30a	1.44	0.21a
12.1	1.94	0.28a	2.90	0.36a	1.87	0.26a

FIGURE CAPTIONS

Fig. 1. Poloidal flux function, Ψ, and toroidal current density contours for the $\beta_p = 0.59$, 1.00, 1.49, and 1.94 equilibria described in Table 1.

Fig. 2. Toroidal current density profiles for the $\beta_p = 0.59$, 1.00, 1.49, and 1.94 equilibria described in Table 1. The dashed lines show the position of the $q = 1$ singular surface.

Fig. 3. $n = 1$ linear growth rate $(\sim\tau_{hp}^{-1})$ vs β_p for the flux conserving sequence of equilibria described in Table 1. The dashed curve includes only the current-driven part of the mode, whereas the solid curve includes the full dynamical effects of the pressure driving terms.

Fig. 4. $m = 1$ components of Ψ, p, and Φ for the $n = 1$ eigenmode for the $\beta_p = 0.19$, 0.59, 1.00, and 1.94 equilibria described in Table 1.

Fig. 5. $m = -2, \ldots, 7$ components of Ψ for the $n = 1$ eigenmode for (a) the $\beta_p = 0.19$ and (b) $\beta_p = 1.94$ equilibria described in Table 1.

Fig. 6. Magnetic energy ratio $(E_M)_{m1}/(E_M)_{11}$ for $m = 2$ and 3. The dashed curves include only the effect of the deformed equilibrium on the current-driven part of the mode, whereas the solid curves also include the full dynamical effects of the pressure driving terms.

Fig. 7. Magnetic energy ratios $(E_M)_{m1}/(E_M)_{11}$ for m = -2, . . . , 7 for (a) the $\beta_p = 0.07$, 0.19, 0.38, 0.59, and 1.00 equilibria described in Table 1 and (b) the $\beta_p = 0.12$, 1.02, and 2.90 equilibria having $q_o = 0.9$ and $q_a = 3.3$ described in Table 2.

Fig. 8. n = 1 linear growth rate $(\sim \tau_{hp}^{-1})$ vs β_o and vs β_p for the flux conserving sequences of equilibria considered here. The solid curve is for $q_o = 0.9$ and $q_a = 2.3$; the long dashed curve is for $q_o = 0.9$ and $q_a = 3.3$; and the short dashed curve is for $q_o = 0.8$ and $q_a = 2.3$.

Fig. 9. n = 1, 3, and 6 linear growth rates $(\sim \tau_{hp}^{-1})$ vs β_p for the flux conserving sequence of equilibria described in Table 1. The value of magnetic Reynolds number $S = 10^4$ was used in the calculation for this figure.

Fig. 10. m = 1/n = 1 magnetic island width (top) and (m = 2;n = 1) poloidal magnetic field fluctuation amplitude at the plasma edge (bottom) vs time for the $\beta_p = 0.07$, 0.19, 0.38, and 0.59 equilibria described in Table 1.

Fig. 11. Magnetic field line plots at $t/\tau_{hp} = 1398$, 1896, 1936, and 1967 for the $\beta_p = 0.38$ case.

Fig. 12. Horizontal and vertical pressure profiles at $t/\tau_{hp} = 0$, 1398, 1896, 1936, and 1967 for the $\beta_p = 0.38$ case.

Fig. 13. Constant pressure contours at $t/\tau_{hp} = 1398$, 1896, 1936, and 1967 for the $\beta_p = 0.38$ case.

Fig. 14. $m = 1/n = 1$ island width vs t/τ_{hp} together with horizontal toroidal current density profile and magnetic field line plot of the saturated state for the $\beta_p = 0.59$ case.

Fig. 15. $m = 1/n = 1$ magnetic island width vs t/τ_{hp} for $S = 10^4$, 10^5, and 10^6 for the $\beta_p = 0.19$ case.

Fig. 16. $m = 1/n = 1$ magnetic island width (top) and $(m = 2;n = 1)$ poloidal magnetic field fluctuation amplitude at the plasma edge (bottom) vs time for the $\beta_p = 0.38$ ($q_o = 0.9$, $q_a = 2.3$) and $\beta_p = 0.34$ ($q_o = 0.9$, $q_a = 3.3$) equilibria described in Tables 1 and 2.

Fig. 17. $m = 1/n = 1$ magnetic island width (top) and $(m = 2;n = 1)$ poloidal magnetic field fluctuation amplitude at the plasma edge (bottom) vs time for the $\beta_p = 0.59$ ($q_o = 0.9$, $q_a = 2.3$) and $\beta_p = 0.57$ ($q_o = 0.8$, $q_a = 2.3$) equilibria described in Tables 1 and 2.

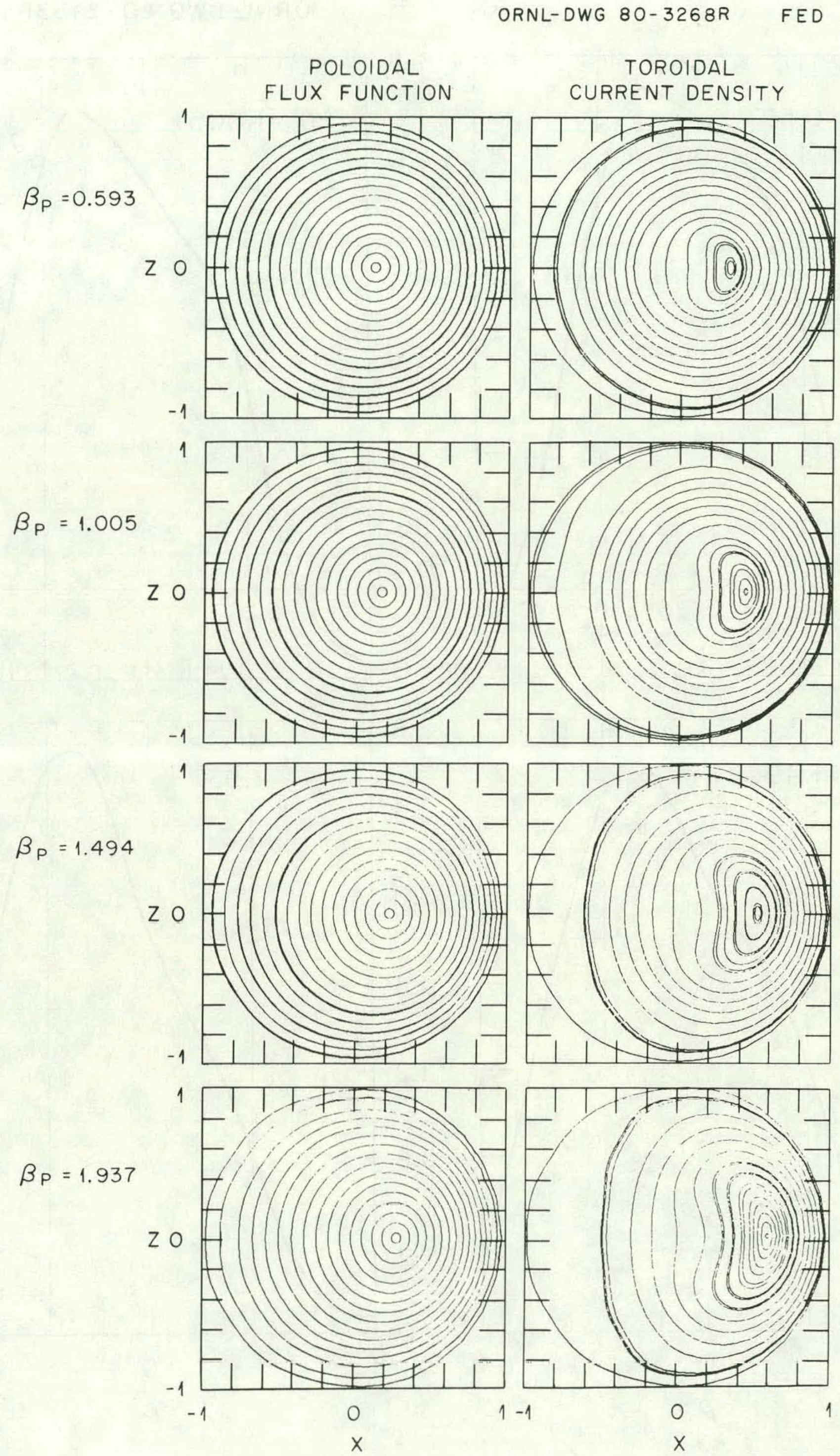
ORNL-DWG 80-3268R FED
POLOIDAL FLUX FUNCTION
TOROIDAL CURRENT DENSITY
β_P = 0.593
β_P = 1.005
β_P = 1.494
β_P = 1.937
Z
0
1
-1
X
-1
0
1

Fig. 1

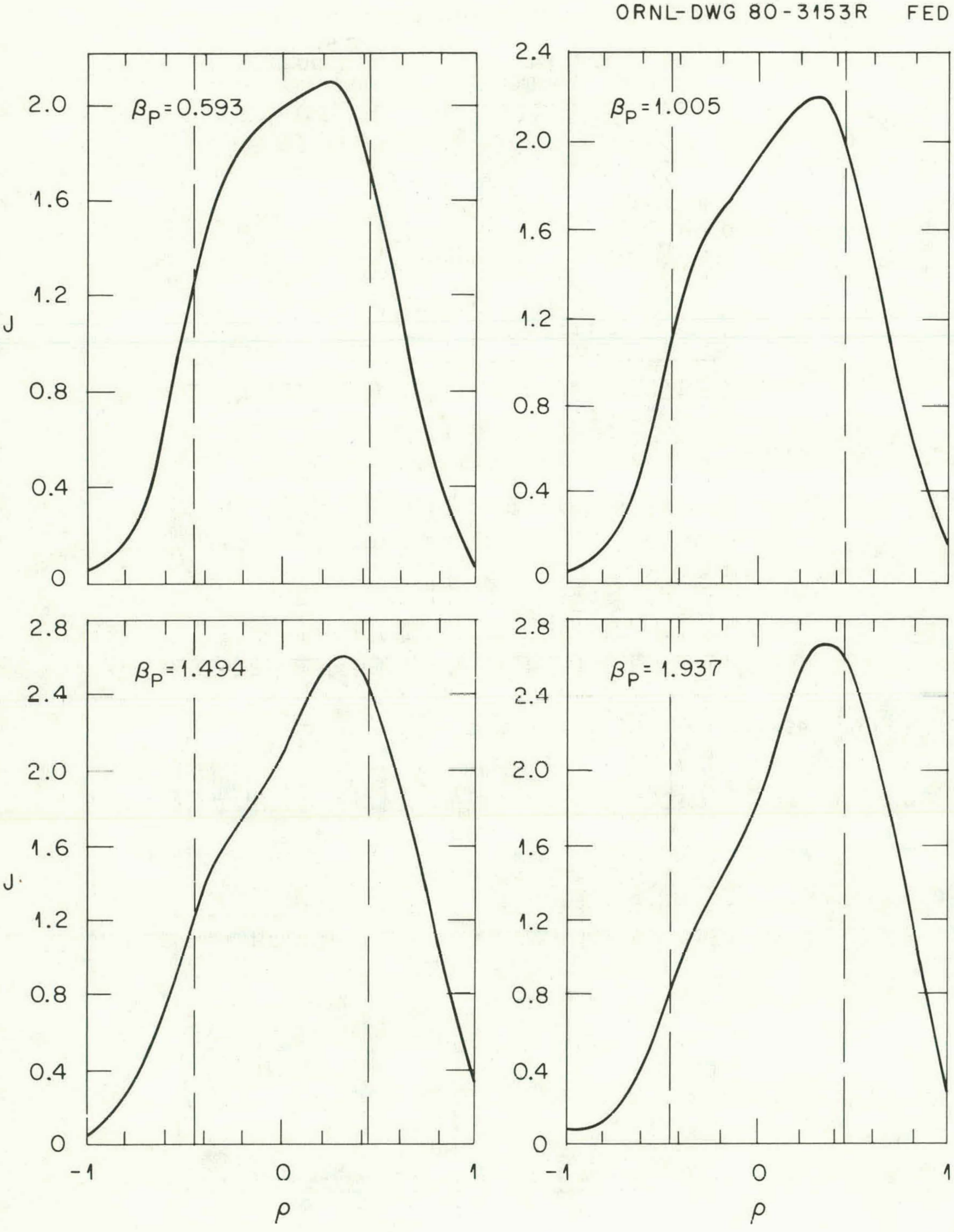
ORNL-DWG 80-3153R FED
β_P=0.593
β_P=1.005
β_P=1.494
β_P=1.937
J
J
0
0.4
0.8
1.2
1.6
2.0
2.4
2.8
-1
0
1
ρ
ρ

Fig. 2

ORNL-DWG 81-3221 FED

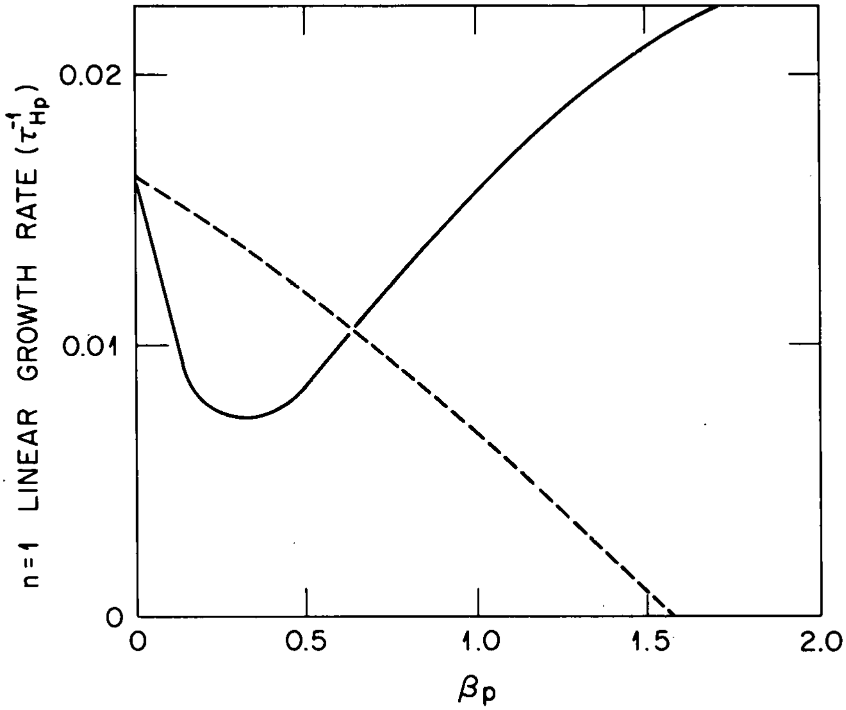

Fig. 3

ORNL-DWG 81-3222 FED

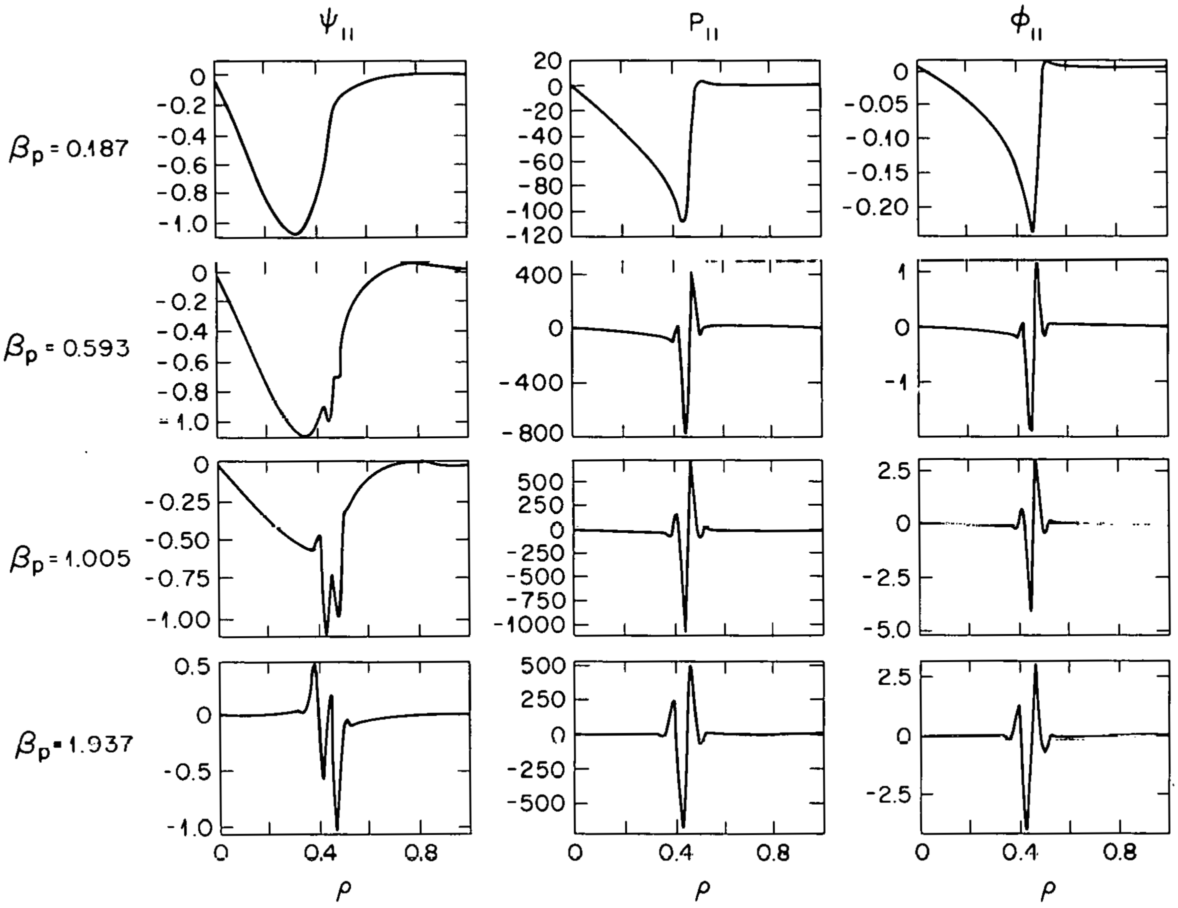

Fig. 4

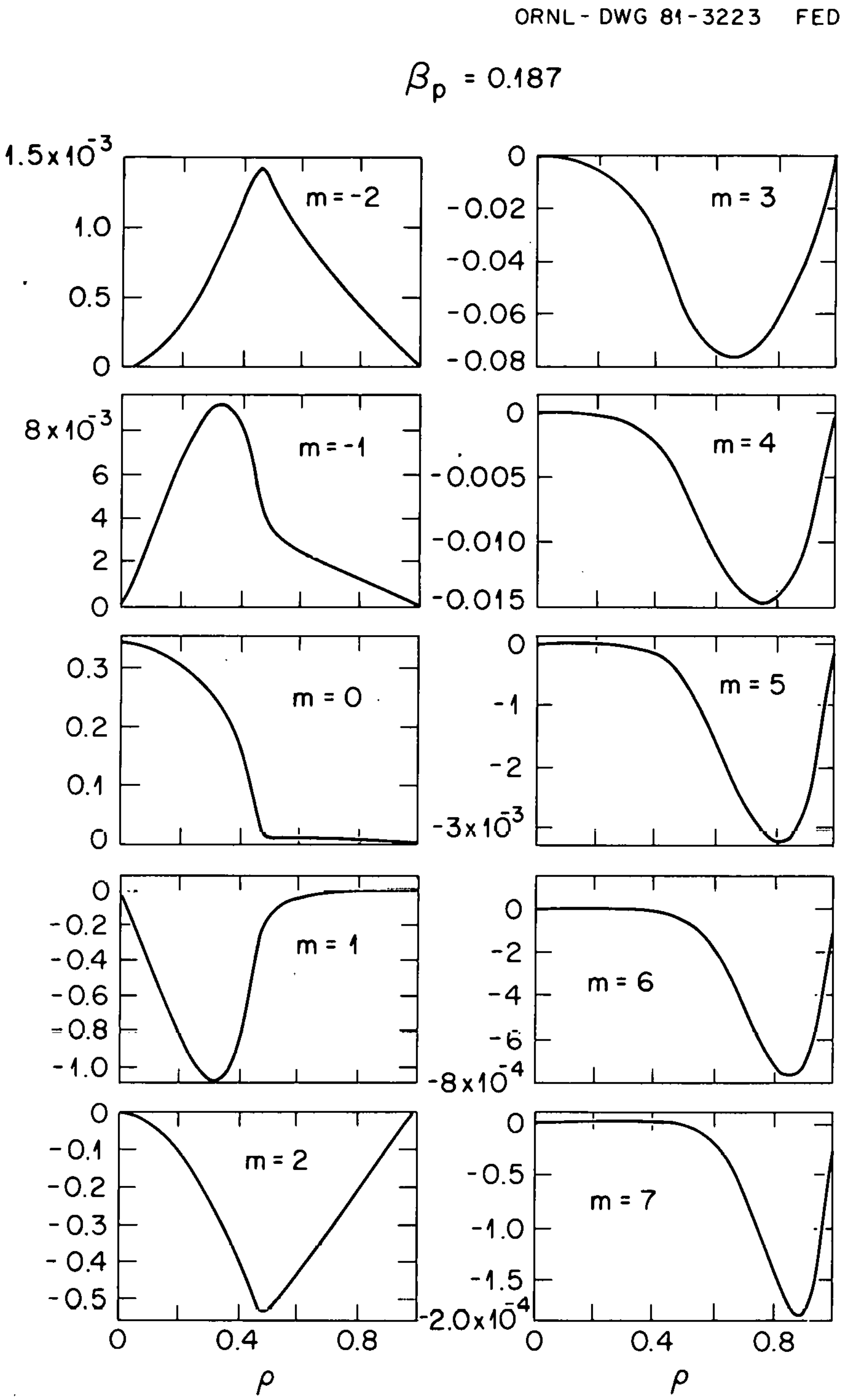
ORNL-DWG 81-3223 FED
β_p = 0.187
m = -2
1.5 x 10^{-3}
1.0
0.5
0
m = -1
8 x 10^{-3}
6
4
2
0
m = 0
0.3
0.2
0.1
0
m = 1
0
-0.2
-0.4
-0.6
-0.8
-1.0
m = 2
0
-0.1
-0.2
-0.3
-0.4
-0.5
0
0.4
0.8
ρ
m = 3
0
-0.02
-0.04
-0.06
-0.08
m = 4
0
-0.005
-0.010
-0.015
m = 5
0
-1
-2
-3 x 10^{-3}
m = 6
0
-2
-4
-6
-8 x 10^{-4}
m = 7
0
-0.5
-1.0
-1.5
-2.0 x 10^{-4}
0
0.4
0.8
ρ

Fig. 5a

ORNL- DWG 81-3224 FED

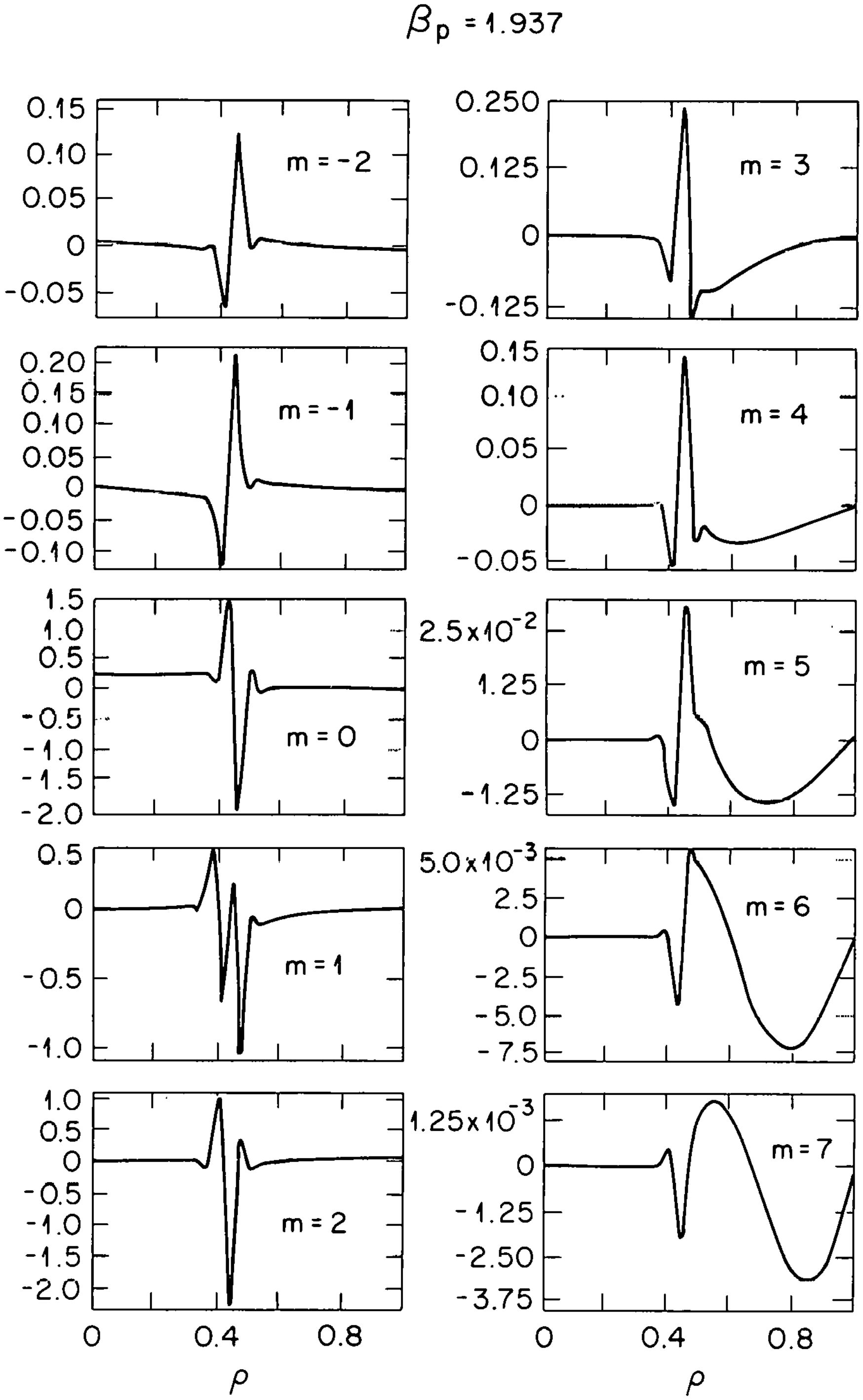
β_p = 1.937
m = -2
0.15
0.10
0.05
0
-0.05
m = -1
0.20
0.15
0.10
0.05
0
-0.05
-0.10
m = 0
1.5
1.0
0.5
0
-0.5
-1.0
-1.5
-2.0
m = 1
0.5
0
-0.5
-1.0
m = 2
1.0
0.5
0
-0.5
-1.0
-1.5
-2.0
m = 3
0.250
0.125
0
-0.125
m = 4
0.15
0.10
0.05
0
-0.05
m = 5
2.5x10^{-2}
1.25
0
-1.25
m = 6
5.0x10^{-3}
2.5
0
-2.5
-5.0
-7.5
m = 7
1.25x10^{-3}
0
-1.25
-2.50
-3.75
0
0.4
0.8
ρ

Fig. 5b

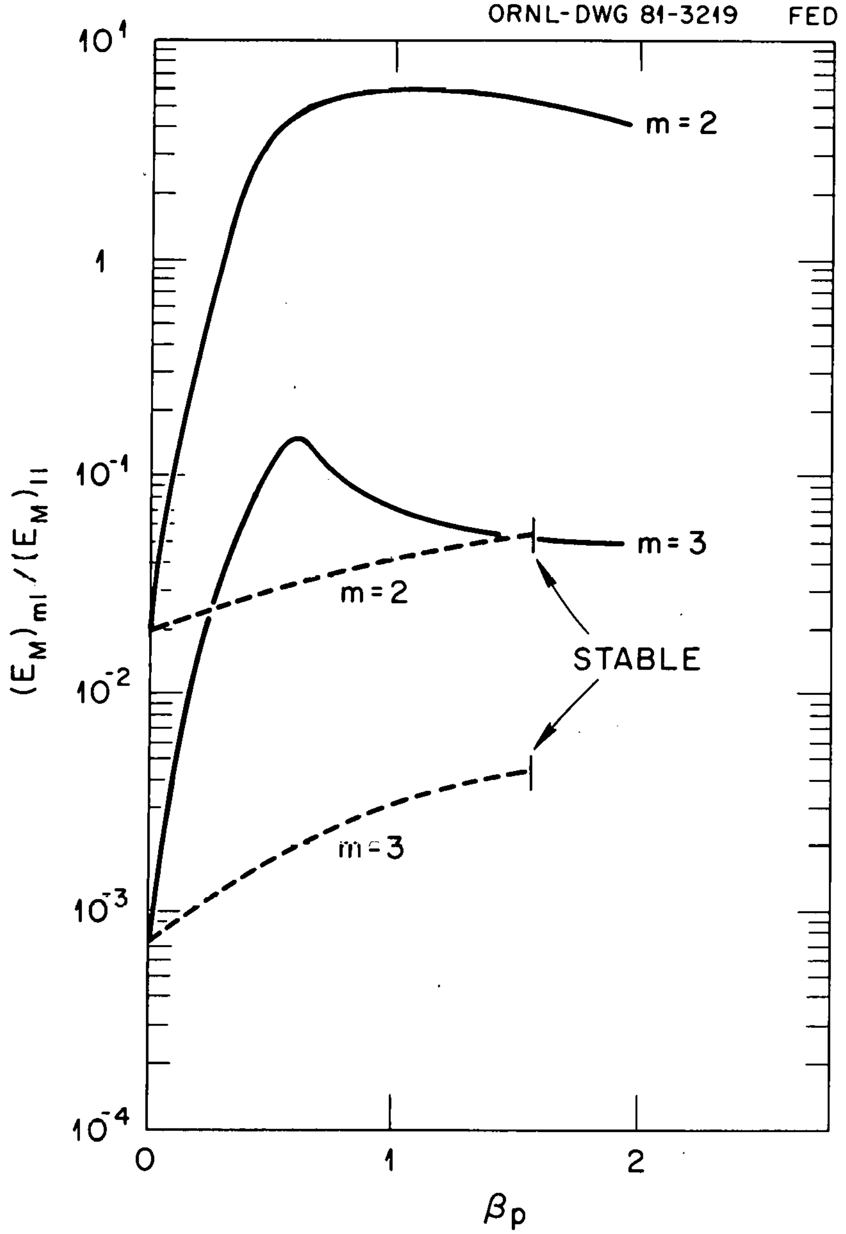
ORNL-DWG 81-3219 FED
10^1
1
10^{-1}
10^{-2}
10^{-3}
10^{-4}
$(E_M)_{ml}/(E_M)_{11}$
0
1
2
β_p
m = 2
m = 3
m = 2
m = 3
STABLE

Fig. 6

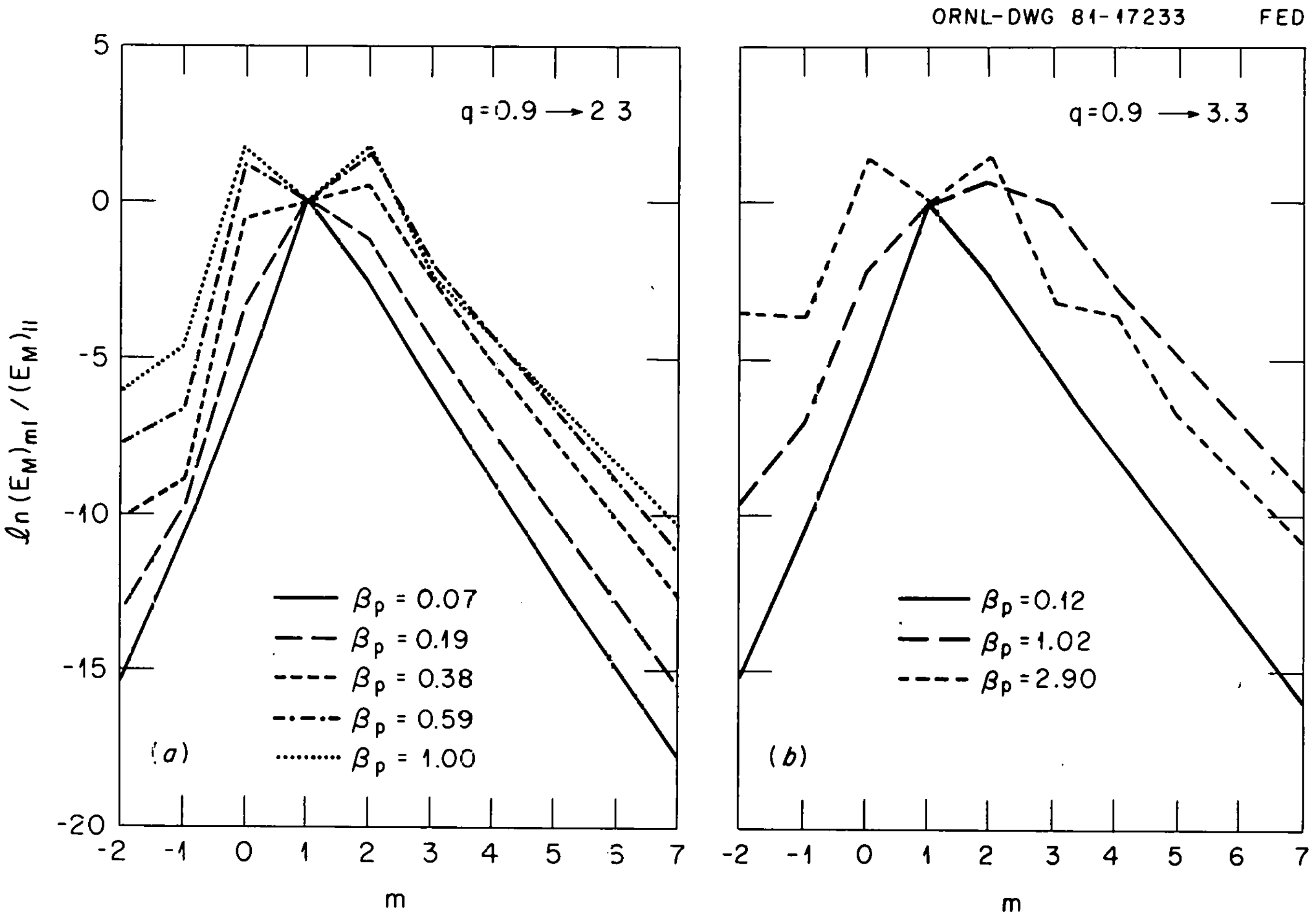
ORNL-DWG 81-17233 FED
q=0.9 → 2 3
q=0.9 → 3.3
$\ell n\,(E_M)_{ml}/(E_M)_{11}$
5
0
-5
-10
-15
-20
-2
-1
0
1
2
3
4
5
6
7
m
β_p = 0.07
β_p = 0.19
β_p = 0.38
β_p = 0.59
β_p = 1.00
(a)
β_p = 0.12
β_p = 1.02
β_p = 2.90
(b)

Fig. 7

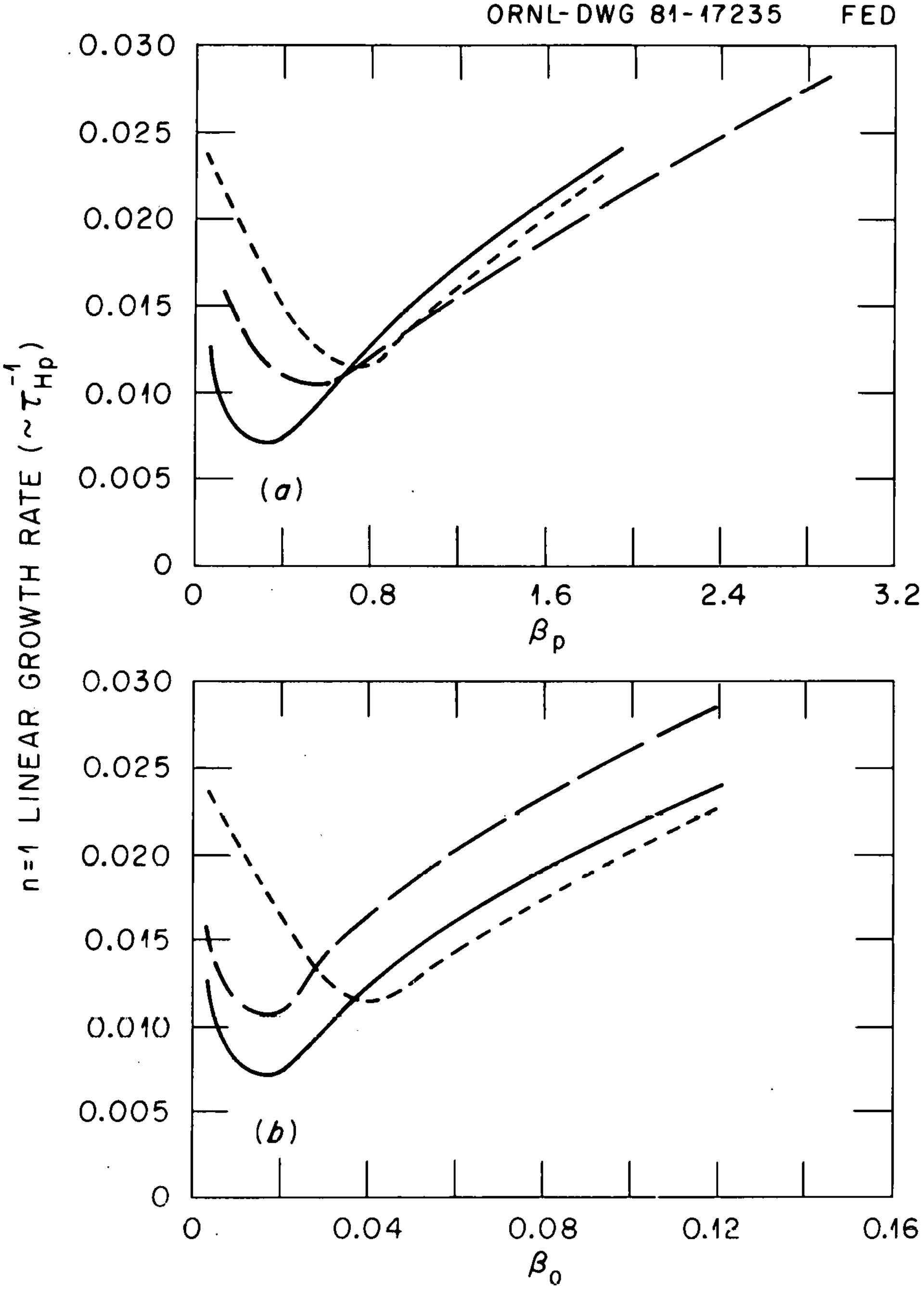
ORNL-DWG 81-17235 FED
0.030
0.025
0.020
0.015
0.010
0.005
0
(a)
0
0.8
1.6
2.4
3.2
β_p
n=1 LINEAR GROWTH RATE ($\sim \tau_{Hp}^{-1}$)
0.030
0.025
0.020
0.015
0.010
0.005
0
(b)
0
0.04
0.08
0.12
0.16
β_0

Fig. 8

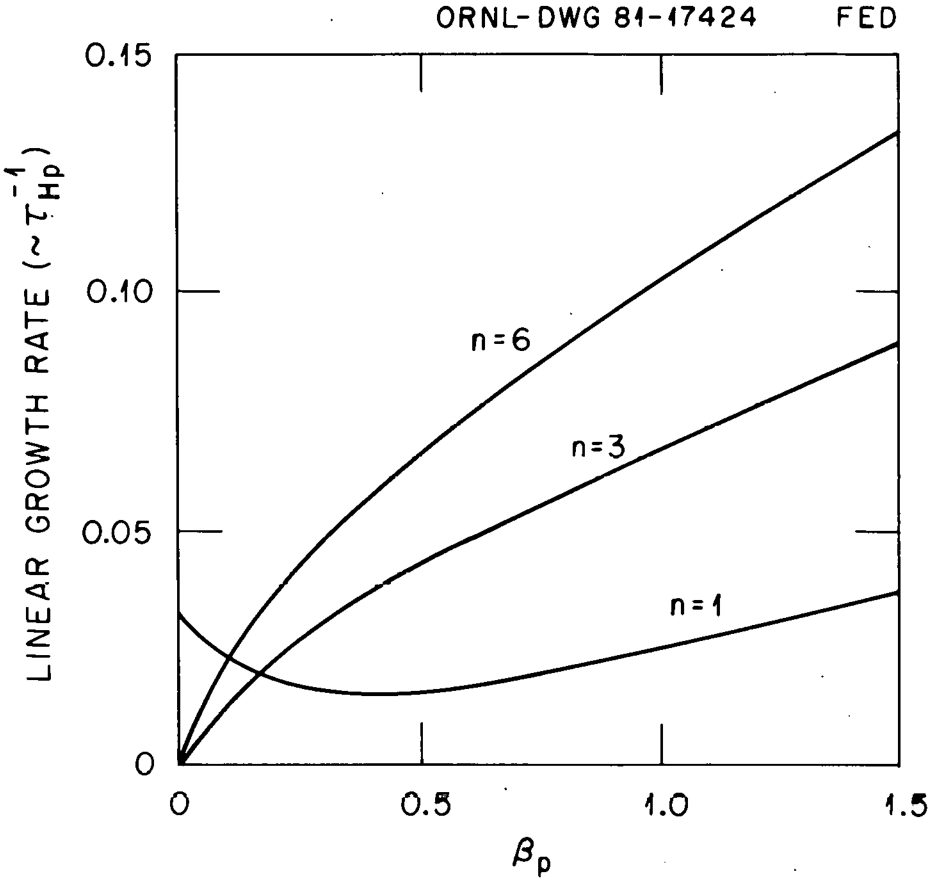
ORNL-DWG 81-17424 FED
LINEAR GROWTH RATE ($\sim \tau_{Hp}^{-1}$)
0.15
0.10
0.05
0
0
0.5
1.0
1.5
β_p
n=6
n=3
n=1

Fig. 9

FINITE β_p EFFECTS:

- SLOWING DOWN THE GROWTH OF THE m=1/n=1 MODE
- COUPLING OF THE m=1 AND m=2 MODES

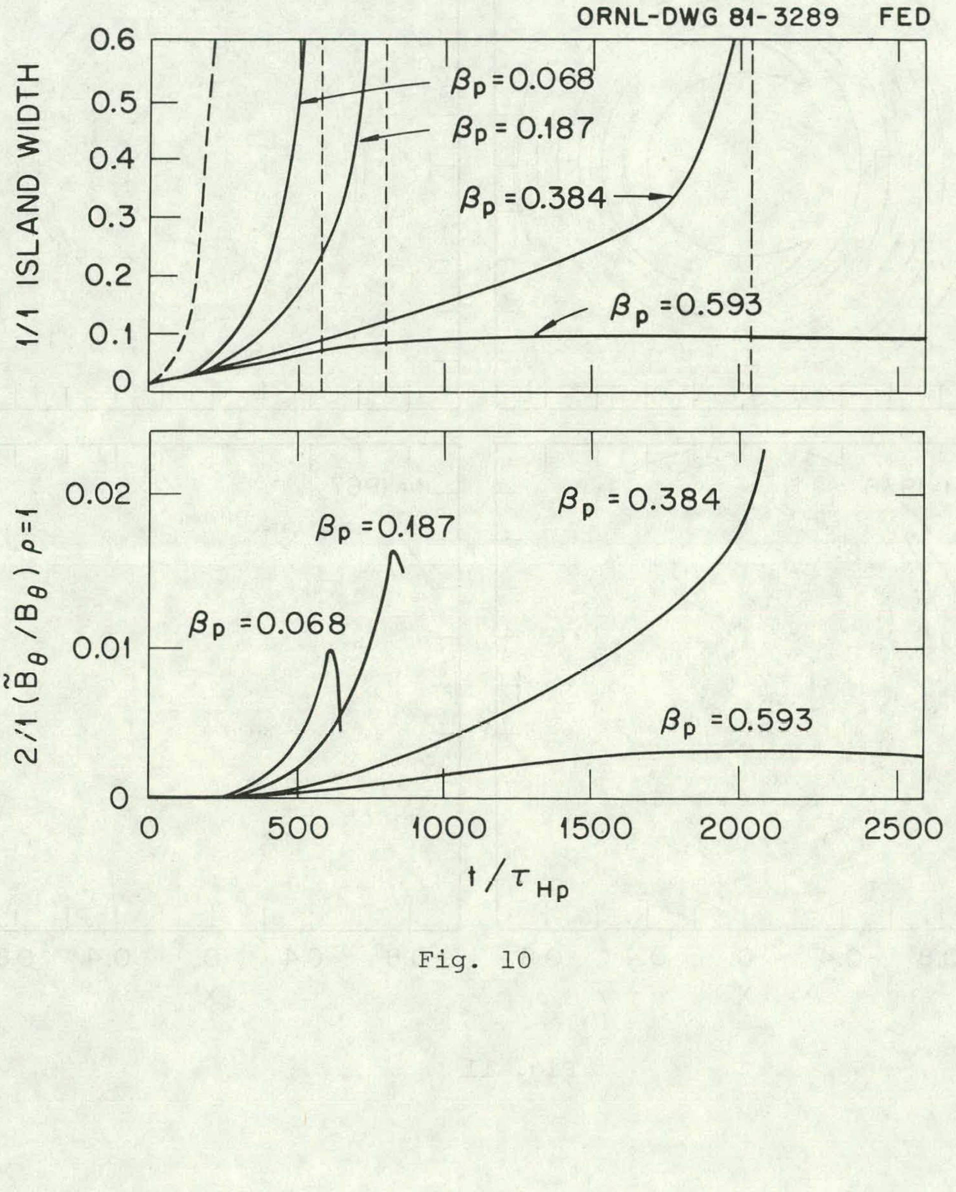

Fig. 10

ORNL-DWG 81-3293 FED

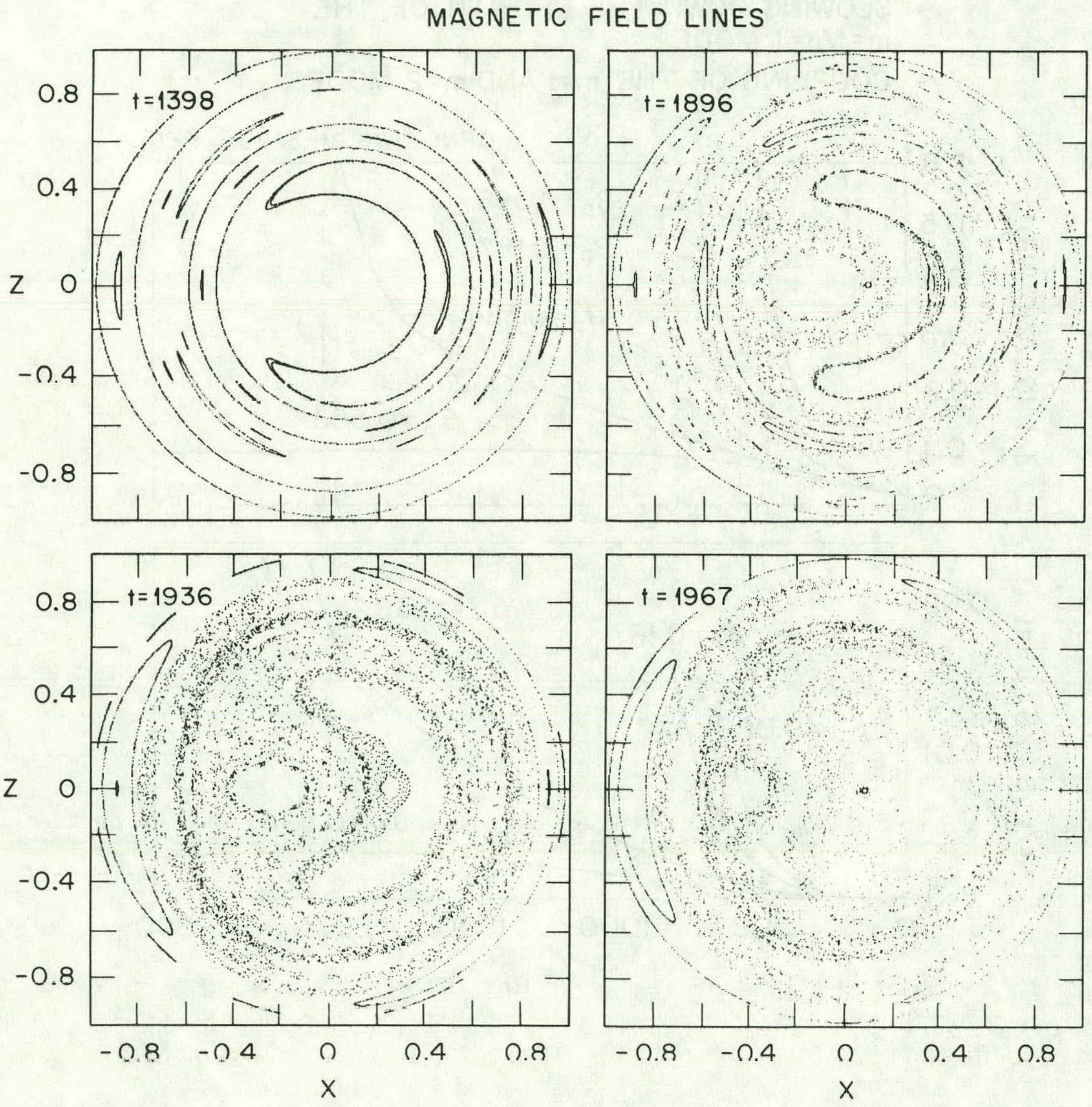

Fig. 11

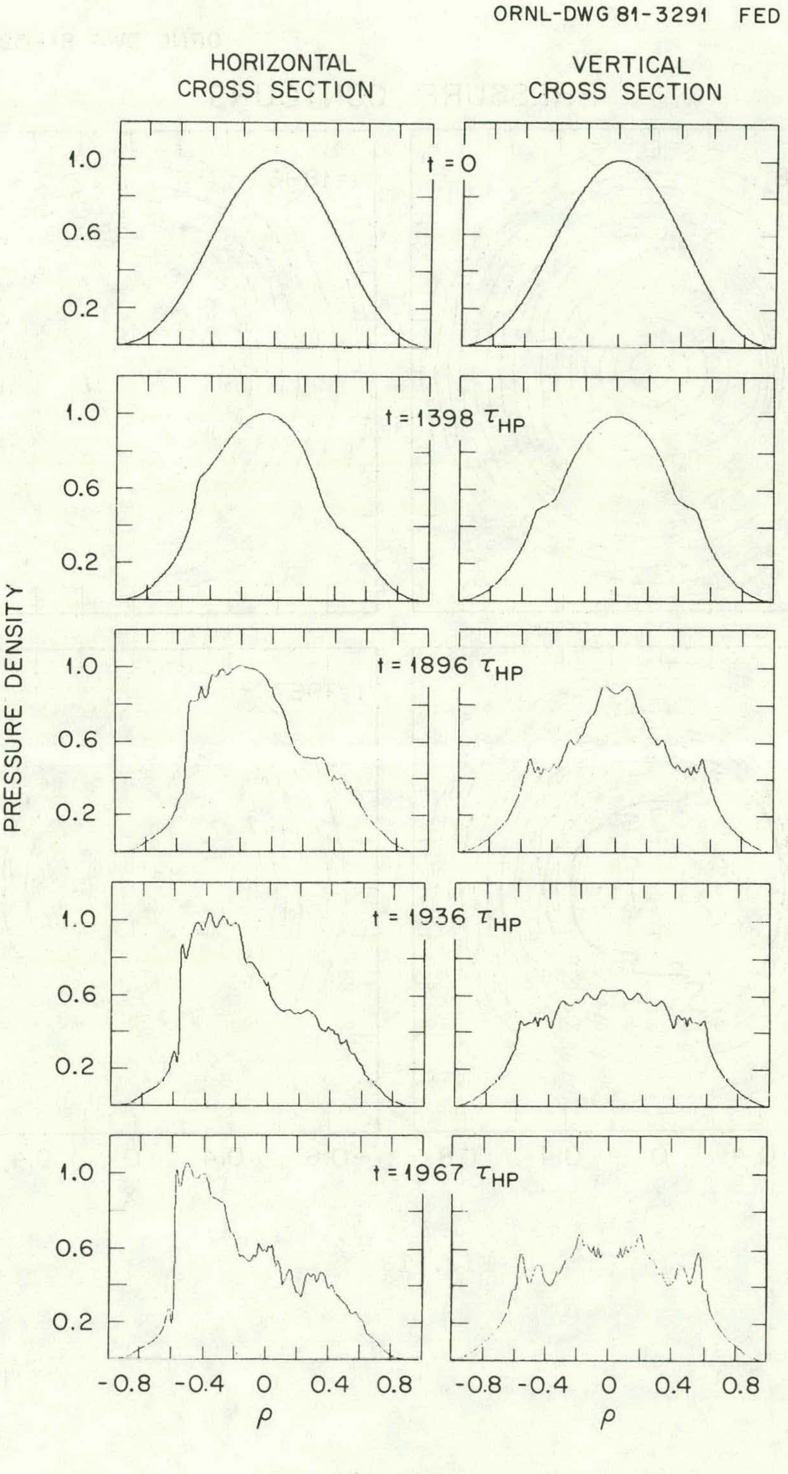
ORNL-DWG 81-3291 FED
HORIZONTAL CROSS SECTION
VERTICAL CROSS SECTION
PRESSURE DENSITY
1.0
0.6
0.2
t = 0
t = 1398 τ_{HP}
t = 1896 τ_{HP}
t = 1936 τ_{HP}
t = 1967 τ_{HP}
-0.8
-0.4
0
0.4
0.8
ρ

Fig. 12

ORNL-DWG 81-3292 FED

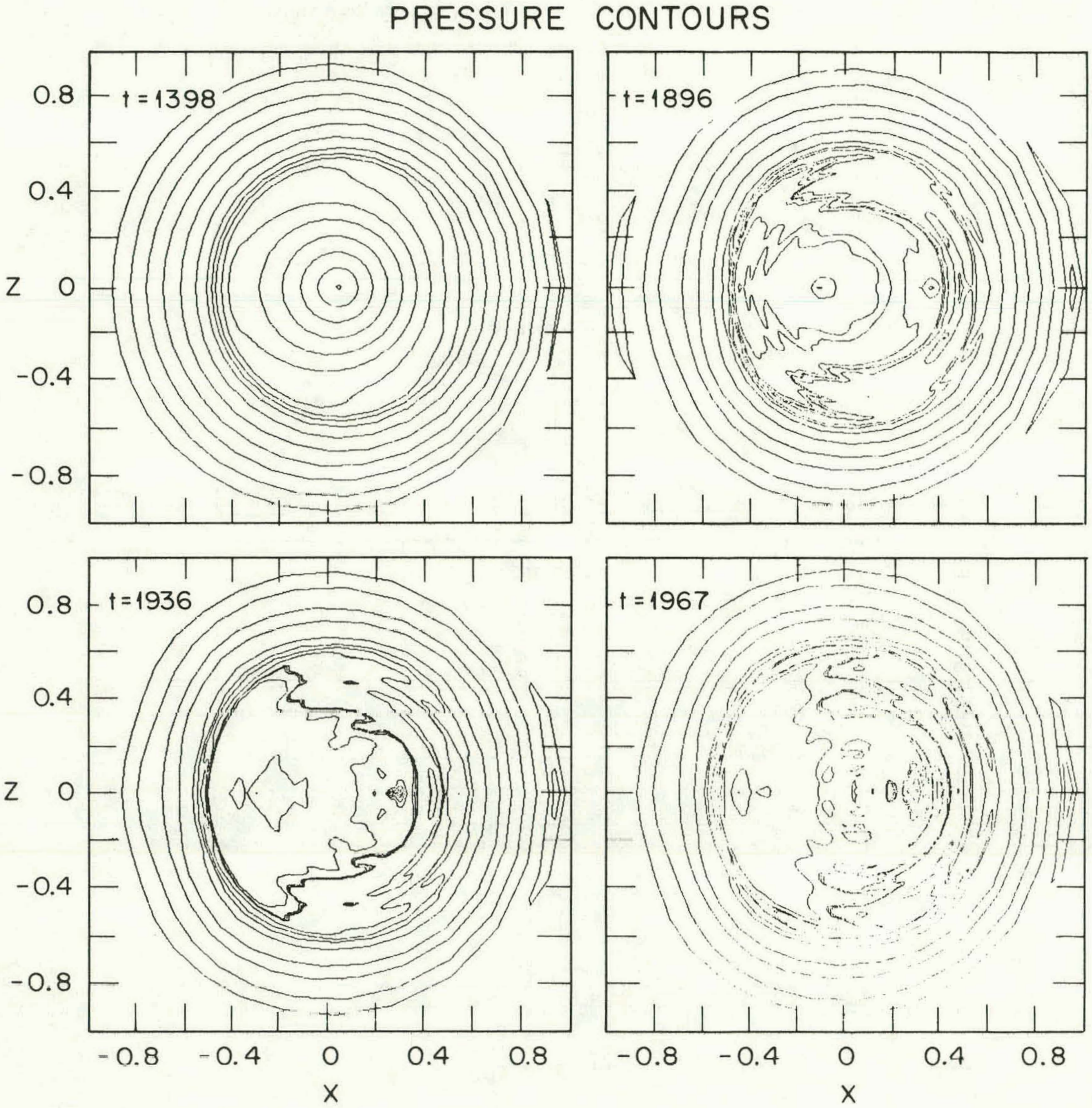

Fig. 13

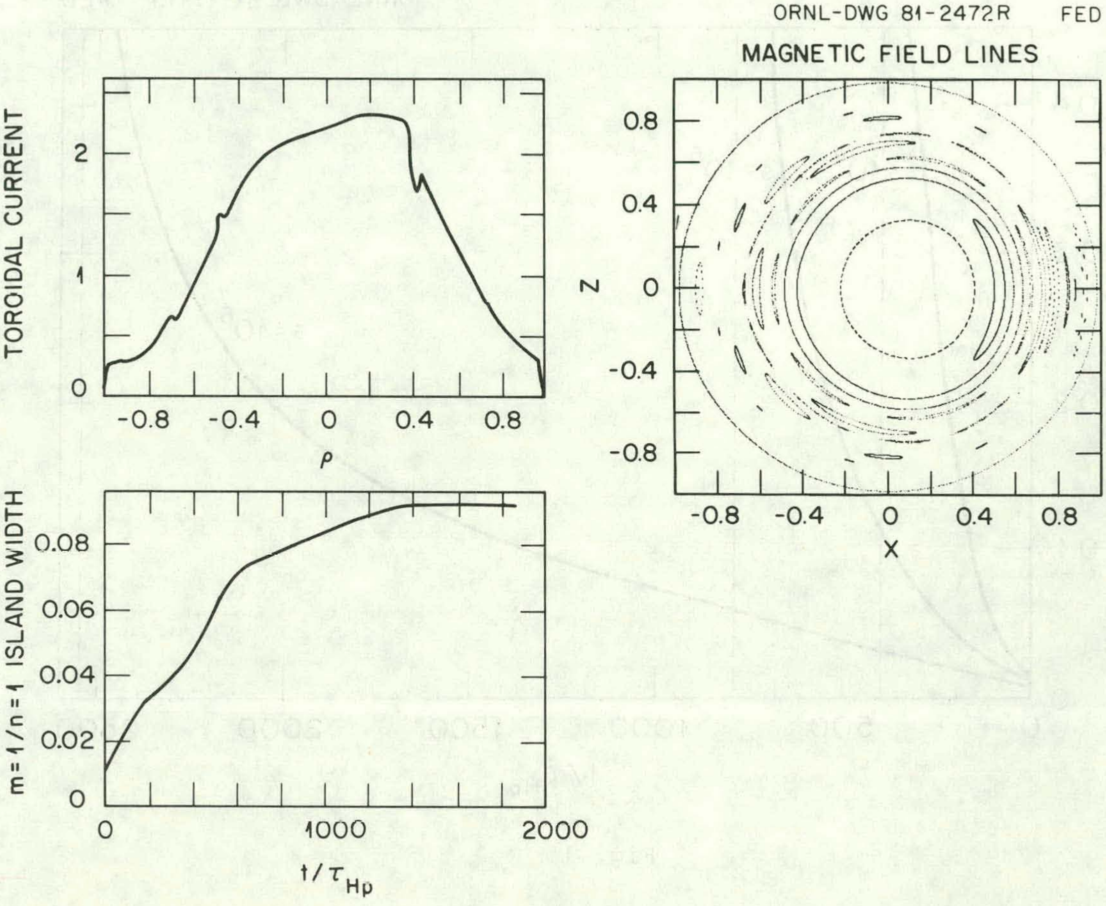
ORNL-DWG 81-2472R FED
MAGNETIC FIELD LINES
TOROIDAL CURRENT
2
1
0
-0.8
-0.4
0
0.4
0.8
ρ
m=1/n=1 ISLAND WIDTH
0.08
0.06
0.04
0.02
0
0
1000
2000
t/τ_Hp
Z
0.8
0.4
0
-0.4
-0.8
-0.8
-0.4
0
0.4
0.8
X

Fig. 14

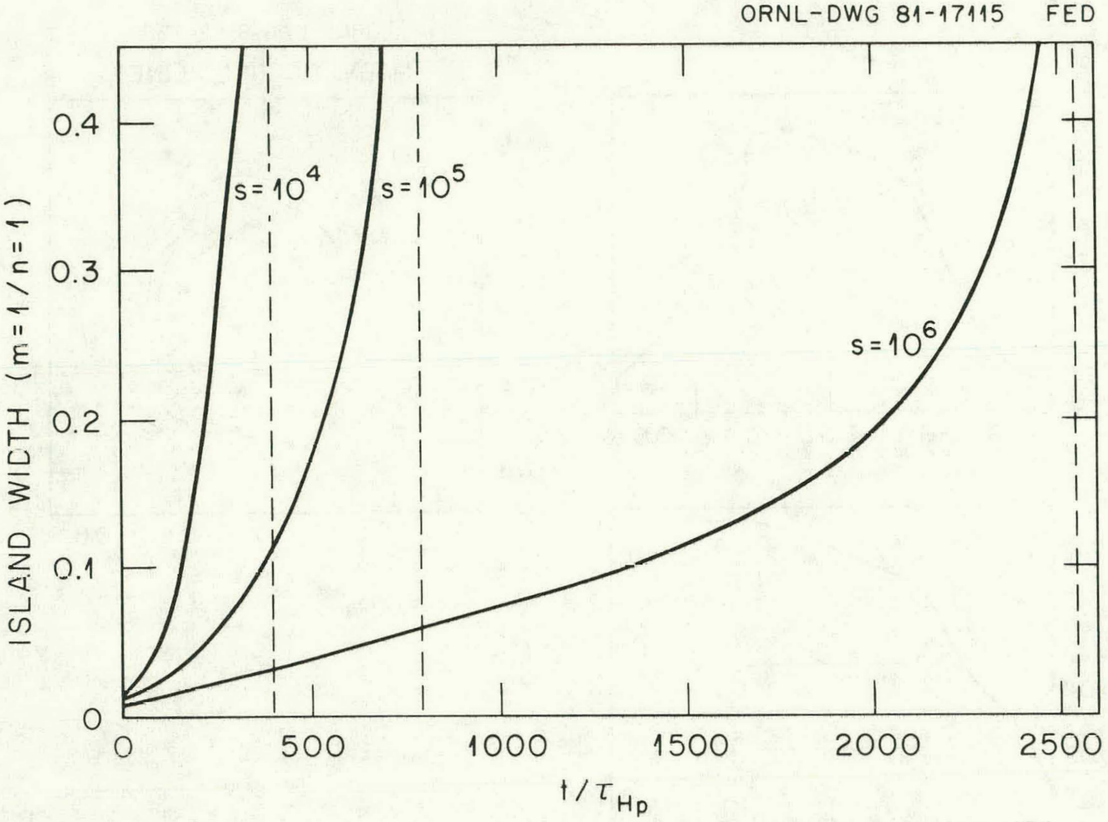
ORNL-DWG 81-17115 FED
ISLAND WIDTH (m=1/n=1)
0.4
0.3
0.2
0.1
0
s=10^4
s=10^5
s=10^6
0
500
1000
1500
2000
2500
t/τ_{Hp}

Fig. 15

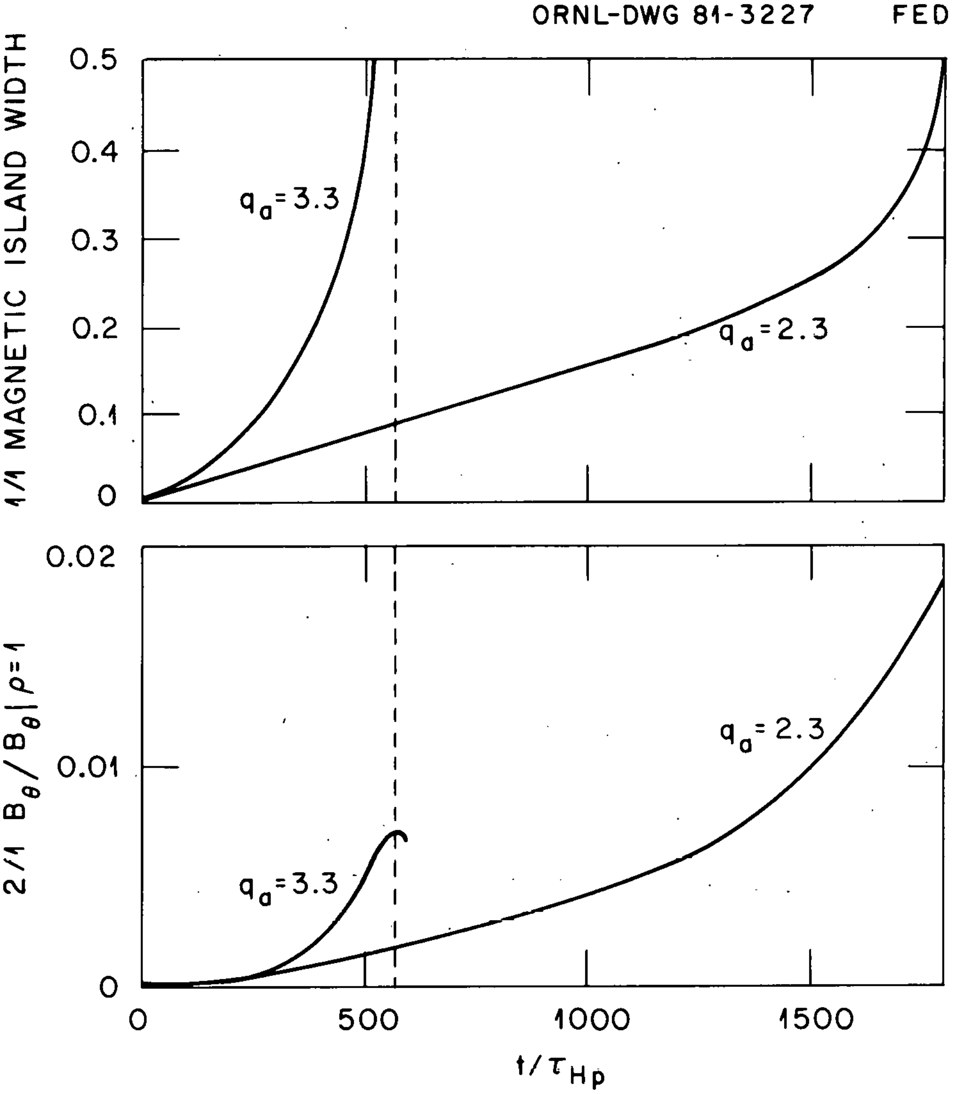
ORNL-DWG 81-3227 FED
1/1 MAGNETIC ISLAND WIDTH
0.5
0.4
0.3
0.2
0.1
0
q_a=3.3
q_a=2.3
0.02
0.01
0
$2/1\ \tilde{B}_\theta/B_\theta|\rho=1$
q_a=2.3
q_a=3.3
0
500
1000
1500
t/τ_{Hp}

Fig. 16

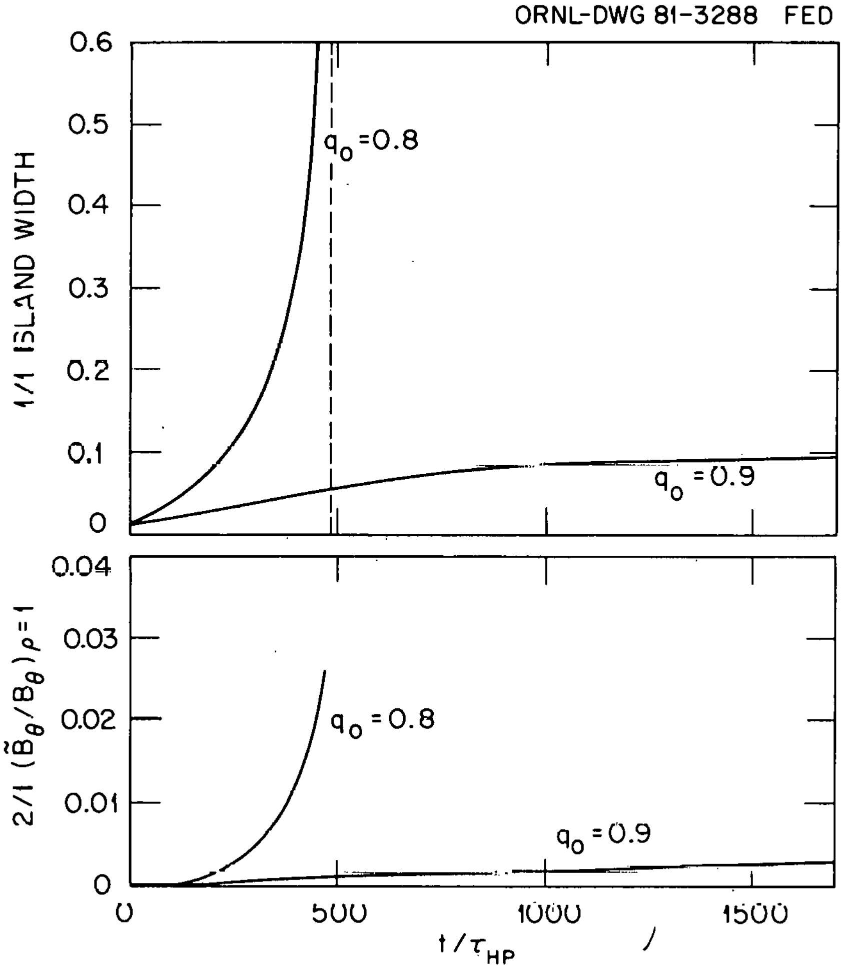

ORNL-DWG 81-3288 FED
0.6
0.5
0.4
0.3
0.2
0.1
0
1/1 ISLAND WIDTH
$q_0=0.8$
$q_0=0.9$
0.04
0.03
0.02
0.01
0
$2/1\ (\tilde{B}_\theta/B_\theta)_{\rho=1}$
$q_0=0.8$
$q_0=0.9$
0
500
1000
1500
t/τ_{HP}

Fig. 17

ORNL/TM-8063
Dist. Category UC-20 g

INTERNAL DISTRIBUTION

1. R. D. Burris
2-6. B. A. Carreras
7. R. A. Dory
8. J. L. Dunlap
9. D. L. Hillis
10-14. J. A. Holmes
15-19. H. R. Hicks
20. W. A. Houlberg
21. E. Lazarus
22-26. V. E. Lynch
27. J. F. Lyon
28. M. Murakami
29. G. H. Neilson
30. Y-K. M. Peng
31. J. A. Rome
32-36. K. E. Rothe
37. M. J. Saltmarsh
38. J. Sheffield
39. G. E. Smith
40. D. A. Spong
41. D. J. Strickler
42. J. B. Wilgen
43-44. Laboratory Records Department
45. Laboratory Records, ORNL-RC
46. Document Reference Section
47-48. Central Research Library
49-50. Fusion Energy Division Library
51. Fusion Energy Division Reports Office
52. ORNL Patent Office

EXTERNAL DISTRIBUTION

53. M. A. Abdou, Argonne National Laboratory, 9700 South Cass Avenue, Argonne, IL 60439
54. D. J. Anthony, Manager, Fusion Energy Systems, General Electric Company, Building 2, Room 551, 1 River Road, Schenectady, NY 12345
55. G. Bateman, Georgia Institute of Technology, Atlanta, GA 30332
56. K. H. Burrell, General Atomic Company, P.O. Box 81608, San Diego, CA 92138
57. J. D. Callen, Department of Nuclear Engineering, 1500 Johnson Drive, University of Wisconsin, Madison, WI 53706
58. G. Clemens, University Library of Essen, Gustav-Hicking Str. 15, D-4300 Essen, Federal Republic of Germany
59. D. R. Cohn, Massachusetts Institute of Technology, Cambridge, MA 02139
60. R. W. Conn, School of Engineering and Applied Science, 6291 Boelter Hall, University of California, Los Angeles, CA 90024
61. Czechoslovak Academy of Sciences Institute of Plasma Physics, Pod Vodarenskou Vezi 4 180 69, Prague 8, Czechoslovakia
62. S. O. Dean, Director, Fusion Energy Development, Science Applications, Inc., 2 Professional Drive, Suite 249, Gaithersburg, MD 20760
63. G. A. Emmert, Department of Nuclear Engineering, 1500 Johnson Drive, University of Wisconsin, Madison, WI 53706
64. H. K. Forsen, Bechtel Group, Inc., Research and Engineering, P.O. Box 3965, San Francisco, CA 94119
65. T. K. Fowler, Associate Director, Magnetic Fusion Energy, Lawrence Livermore National Laboratory, P.O. Box 808, Livermore, CA 94550

66. R. Goldston, Princeton Plasma Physics Laboratory, P.O. Box 451,
Princeton, NJ 08540
67. G. E. Guest, General Atomic Company, P.O. Box 81608, San Diego,
CA 92138
68. J. Hosea, Princeton Plasma Physics Laboratory, P.O. Box 451,
Princeton, NJ 08540
69. P-Y. S. Hsu, EG&G Idaho, Idaho National Engineering Laboratory,
P.O. Box 1625, Idaho Falls, ID 83401
70. R. Jones, Department of Physics, National University of Singapore,
Bukit Timah Road, Singapore
71. G. L. Kulcinski, Nuclear Engineering Department, 1500 Johnson
Drive, University of Wisconsin, Madison, WI 53706
72. R. L. Miller, General Atomic Company, P.O. Box 81608, San Diego,
CA 92138
73. D. B. Montgomery, Massachusetts Institute of Technology,
Cambridge, MA 02139
74. D. Overskei, Massachusetts Institute of Technology, Cambridge,
MA 02139
75. F. Perkins, Princeton Plasma Physics Laboratory, P.O. Box 451,
Princeton, NJ 08540
76. J. M. Rawls, General Atomic Company, P.O. Box 81608, San Diego,
CA 92138
77. P. H. Rutherford, Princeton Plasma Physics Laboratory, P.O. Box
451, Princeton, NJ 08540
78. J. A. Schmidt, Princeton Plasma Physics Laboratory, P.O. Box 451,
Princeton, NJ 08540
79. W. M. Stacey, Georgia Institute of Technology, Atlanta, GA 30332
80. W. Stodiek, Princeton Plasma Physics Laboratory, P.O. Box 451,
Princeton, NJ 08540
81. D. P. Tewari, Department of Physics, Indian Institute of
Technology, New Delhi 110016, India
82. Office of Assistant Manager for Energy Research and Development,
Department of Energy, Oak Ridge Operations, Oak Ridge, TN 37830
83-258. Given distribution as shown in TID-4500, Magnetic Fusion Energy
(Distribution Category UC-20 g, Theoretical Plasma Physics)